

**An improved methodology to estimate cross-scale kinetic energy transfers  
from third-order structure functions using regularized least-squares**

Manuel O. Gutierrez-Villanueva,<sup>a</sup> Bruce D. Cornuelle,<sup>b</sup> Sarah T. Gille,<sup>b</sup> Matthew R. Mazloff,<sup>b</sup>  
Dhruv Balwada,<sup>a</sup>

<sup>a</sup> *Lamont-Doherty Earth Observatory, Columbia University, Palisades, NY*

<sup>b</sup> *Scripps Institution of Oceanography, University of California San Diego, La Jolla, CA*

*Corresponding author:* Manuel O. Gutierrez-Villanueva, mg4864@columbia.edu

8 ABSTRACT: Several methods exist for estimating cross-scale kinetic energy (KE) transfers; how-  
9 ever, most are ill-adapted for sparse ocean observations, hindering the study of oceanic KE transfers.  
10 A newly developed third-order structure function,  $D3(r)$ , framework allows estimation of KE injec-  
11 tions  $\xi_j(k)$  and spectral flux  $F(k)$  across scales using sparse data. This approach requires inverse  
12 methods to convert between separation  $r$  and wavenumber  $k$  space. A previous study employed  
13 the structure-function framework to estimate  $F(k)$  and  $\xi_j(k)$  using non-negative least squares  
14 (NNLS), assuming that the spectral flux is an increasing function of wavenumber, an assumption  
15 not always satisfied. Here, an improved methodology is presented to estimate  $F(k)$  and  $\xi_j$  using  
16 regularized least-squares (RLS), where the inclusion of prior uncertainty in  $D3(r)$  and  $\xi_j$  reduces  
17 overfitting. Moreover, the improved methodology allows for estimating both positive and negative  
18 injections without making assumptions about the shape of the spectral flux. As a proof of concept,  
19 the improved methodology was implemented in an eddy-rich quasi-geostrophic simulation output.  
20 RLS quantitatively diagnoses the structure of  $F(k)$ , including both positive and negative  $\xi_j(k)$ ,  
21 an aspect unattainable with NNLS. The improved methodology was then applied to data from  
22 two drifter experiments in the Gulf of Mexico. The analysis reveals the presence of bidirectional  
23 energy transfers, with a KE inverse transfer at mesoscales in both seasons and a forward transfer  
24 at submesoscales that is stronger in winter than in summer. Unlike NNLS, RLS fits  $D3(r)$  better  
25 as the method detects wavenumbers where  $\xi_j < 0$  while preserving smoothness. This improved  
26 methodology allows for a more refined analysis of KE transfers from sparse observations.

## 27 1. Introduction

28 Cross-scale kinetic energy (KE) transfers play a key role in several aspects of ocean circulation  
29 (Ferrari and Wunsch 2009), as they mediate the flow of energy from the scales where it is injected  
30 through atmospheric forcing, tides, and solar heating to the scales where it is ultimately dissipated  
31 by molecular viscosity. Quasi-geostrophic turbulence theory, a cornerstone of classical ocean  
32 dynamics, suggests that at mesoscales,  $O(50-200)$  km, energy is transferred on average toward  
33 larger scales (inverse cascade), and satellite observations provide strong evidence to support this  
34 (Scott and Wang 2005; Vallis 2017). Recently, a new body of numerical and observational work  
35 has suggested that energy at submesoscales  $O(1-10)$  km may be transferred downscale (forward  
36 cascade) en route to dissipation (Schubert et al. 2020; Balwada et al. 2022; Freilich et al. 2023;  
37 Tedesco et al. 2024; Naveira Garabato et al. 2022). It has also been suggested that mesoscale and  
38 submesoscale flows interact by exchanging energy (Sasaki et al. 2017; Steinberg et al. 2022) and  
39 that these interactions may help modulate how oceanic flows redistribute heat, carbon, and other  
40 tracers in the global ocean, with important consequences for global climate (Balwada et al. 2021;  
41 Zhang et al. 2023).

42 Several methods exist to study the energy transfer across scales when gridded data from numerical  
43 simulations or mapped observations are available. The most commonly used are spectral methods,  
44 which have traditionally been used for estimating KE transfers from gridded velocity fields by  
45 considering the Fourier transform in wavenumber space (e.g. Capet et al. 2008; Ajayi et al. 2021;  
46 Dong et al. 2020). In addition to requiring uniformly gridded data, spectral methods also require that  
47 data be preprocessed by removing spatiotemporal means and windowing to minimize edge effects  
48 in nonperiodic domains, which can quantitatively and qualitatively impact the estimated transfer  
49 (Aluie et al. 2018). Also, the estimated transfers are obtained as bulk or non-local estimates over  
50 the entire study domain, and localized details cannot be inferred. Using wavelets instead of Fourier  
51 transforms allows local properties to be probed but still entails similar pre-processing (Uchida et al.  
52 2023). More recently, a coarse-graining approach has been introduced in oceanography (Aluie  
53 et al. 2018), which parses flow at different scales with the help of filtering (e.g., top-hat filter). This  
54 method also relies on gridded data but has the advantage of estimating the cross-scale transfers at  
55 each location, similar to wavelets, and avoids the need to artificially impose periodicity (Aluie et al.  
56 2018; Srinivasan et al. 2023; Freilich et al. 2023; Naveira Garabato et al. 2022; Tedesco et al. 2024;

Schubert et al. 2023, 2020; Storer et al. 2023; Yu et al. 2024). Since all these approaches depend on gridded data, they are technically challenging to implement with sparse or non-uniformly sampled observations, impeding their use to study KE transfers in the real ocean.

An alternative to relying on gridded information for estimating KE transfers involves using third-order velocity structure functions. Third-order structure functions are foundational in three-dimensional turbulence theory. In particular, when kinetic energy cascades downscale at a rate of  $\epsilon$  within the inertial range (i.e., scales away from direct forcing and viscous dissipation), the theory predicts the exact result  $\langle \delta u_L^3(r) \rangle = -\frac{4}{5}\epsilon r$ , known as Kolmogorov’s four-fifths law (Kolmogorov 1991). Here  $r$  is the two-point separation distance,  $\delta u_L$  is the longitudinal velocity increment ( $\delta u_L^n \equiv (\delta u_L)^n$  indicates the  $n$ th power of the increment), and  $\langle \cdot \rangle$  denotes an ensemble average. Although this exact law is unlikely to hold in more complex, realistic scenarios, the sign of the third-order structure function has been widely employed as a heuristic tool to infer the direction of energy transfer in studies of natural flows (Lindborg 1999; Lindborg and Cho 2001; Cho and Lindborg 2001; Qiu et al. 2022; Balwada et al. 2016; Poje et al. 2017). However, this heuristic approach faces limitations due to challenges in identifying inertial ranges in oceanic flows and determining the turbulence regime (e.g., 2D, 3D, or quasi-geostrophic). These uncertainties undermine the robustness of  $\epsilon$  estimates when the underlying assumptions are violated.

A recently developed framework by Xie and Bühler (2019) employs third-order structure functions to estimate the energy injection rates across multiple forcing scales and the spectral flux. The new framework does not require identifying inertial ranges and can be applied to scattered and heterogeneous data under assumptions of axisymmetry (isotropy) and homogeneity. Balwada et al. (2022) implemented this methodology using a piecewise function for the spectral flux to estimate the structure of KE transfers in spectral space, using two drifter datasets collected in summer and winter that resolve submesoscale flows down to  $O(100)$  m. They employed a non-negative least-squares (NNLS) method to invert the third-order structure functions and estimate KE injection rates and spectral flux. However, the NNLS method inherently cannot capture negative KE injection rates (indicative of KE transfer convergence in spectral space). As a result, the derived KE transfers are strictly increasing with wavenumber, an assumption that may not hold universally, such as during the conversion of KE to potential energy.

Here, we improve on the estimation of the KE transfers presented by Balwada et al. (2022) by utilizing regularized least-squares (RLS) (e.g. Wunsch 1996; Kachelein et al. 2022). The RLS approach allows us to 1) prescribe a prior uncertainty in the KE injection rates, reducing overfitting in the inversion problem that leads to non-physical energy transfers when using ordinary least-squares, 2) propagate the uncertainty in the estimated third-order structure functions to the calculated KE transfers and injection rates, 3) make no assumptions regarding the direction of the KE transfers, and thus 4) potentially identify energy sinks.

To demonstrate the success of RLS in estimating KE transfers, we first use an idealized two-layer quasi-geostrophic (QG) model that generates mesoscale eddies. In this scenario, energy is injected into the flow, transferred to the larger-scale flows, and dissipated at larger scales through bottom drag. We show that the RLS method resolves the expected shape of the KE transfers as it resolves KE sinks (negative KE injection density per wavenumber) that are otherwise unresolved by the NNLS method, as the latter is incapable of estimating negative injection rates. We then apply this methodology to drifter data from two targeted experiments in the Gulf of Mexico (Balwada et al. 2022), improving the estimates of the bidirectional transfers and its seasonality. The results confirm an inverse transfer at mesoscales and a forward transfer at submesoscales, modulated by seasonal energy injection. Unlike NNLS, RLS fits the estimated third-order structure function better, as it captures KE sinks. The paper is organized as follows: Section 2 reviews the structure-function and KE transfer theory. The improved methodology is explained in Section 3. Details of the QG model setup, the drifter data, and the steps to estimate structure functions are presented in Section 4. Results from the QG model are presented in Section 5a, while Section 5b explores drifter experiments and compares estimates with prior studies. Also, Section 5 presents sample distributions of the third-order structure function, along with the steps taken to estimate prior uncertainties in both the structure function and injection rates. Section 6 concludes with a summary of the improved methodology's results, advantages, and limitations.

## 2. Structure Function Framework

Structure functions provide a powerful framework for diagnosing ocean energetics from sparse observations. The foundation of this approach is the estimation of two-point differences in scalars

or vectors, such as velocity differences:

$$\delta \mathbf{u}(\mathbf{s}, \mathbf{r}, t) = \mathbf{u}(\mathbf{s} + \mathbf{r}, t) - \mathbf{u}(\mathbf{s}, t), \quad (1)$$

where  $\delta \mathbf{u}$  represents the velocity difference between two points  $\mathbf{s}$  and  $\mathbf{s} + \mathbf{r}$  separated by the vector  $\mathbf{r}$  at time  $t$ . These velocity differences are the central focus of this study. To avoid reliance on fixed geographical coordinates, we decompose  $\delta \mathbf{u}$  into longitudinal and transverse components  $\delta \mathbf{u} = (\delta u_L, \delta u_T)$ :

$$\delta u_L = \delta \mathbf{u} \cdot \frac{\mathbf{r}}{|\mathbf{r}|}, \quad \delta u_T = \frac{\hat{\mathbf{z}} \cdot (\delta \mathbf{u} \times \mathbf{r})}{|\mathbf{r}|}, \quad (2)$$

where  $\hat{\mathbf{z}}$  is the vertical unit vector.

#### *a. First- and second-order velocity structure functions*

Given a sample set of velocity differences across many random pairs, velocity structure functions are defined as raw statistical moments of these random variables. Here we defined the first-order structure function  $D1(r)$  for stationary, homogeneous and isotropic flows as:

$$D1(r) = D1_L(r) + D1_T(r) = \langle \delta u_L(\mathbf{s}, \mathbf{r}, t) \rangle + \langle \delta u_T(\mathbf{s}, \mathbf{r}, t) \rangle, \quad (3)$$

where  $r = |\mathbf{r}|$ , and  $\langle \cdot \rangle$  represents the ensemble average over all members of the ensemble at each  $r$ . Often, in practice, and when the assumptions of stationarity, isotropy, and homogeneity approximately hold, ensemble averaging is replaced by averaging over all samples corresponding to a spatio-temporal average. Also, we chose to define  $D1(r)$  as a sum of the longitudinal  $D1_L(r)$  and transverse  $D1_T(r)$  components, but other choices with different interpretations are also valid.  $D1(r)$  provides a measure of the strength of the gradients in the mean flow and is rarely discussed in the theoretical literature that often assumes that the background mean flow is zero or constant.

Similarly, the second-order structure is defined as,

$$D2(r) = D2_{LL}(r) + D2_{TT}(r) = \langle \delta u_L^2(\mathbf{s}, \mathbf{r}, t) \rangle + \langle \delta u_T^2(\mathbf{s}, \mathbf{r}, t) \rangle, \quad (4)$$

which is a sum of the longitudinal and transverse components, denoted as  $D2_{LL}(r)$  and  $D2_{TT}(r)$ , respectively.  $D2(r)$  provides a measure of the energy within the isotropic, stationary 2D flow at a

scale  $r$  and can be precisely connected to the isotropic KE spectrum  $E(k)$  as:

$$D2(r) = 2 \int_0^\infty E(k) [1 - J_0(kr)] dk, \quad (5)$$

where  $J_0$  is the zeroth-order Bessel function (Bennett 1984),  $k = \sqrt{k_x^2 + k_y^2}$  is the isotropic wavenumber ( $k_x$  and  $k_y$  are the zonal and meridional wavenumbers, respectively), and  $dk$  is the wavenumber resolution. Assuming the existence of a KE spectrum that follows a power law  $E(k) \sim k^{-\theta}$ , one can show using (5) that the second-order structure function has a form of  $D2(r) \sim r^{\theta-1}$  where  $\theta$  is the wavenumber spectral slope (Bennett 1984).

#### *b. Third-order structure function and cross-scale KE transfers*

At the third order, we follow Balwada et al. (2022), employing the theoretical framework of Xie and Bühler (2019), who derived a formulation (from the Karman–Howarth–Monin equation) capable of capturing bidirectional KE transfers by using the calculated isotropic third-order structure function. The longitudinal component of the third-order structure function is defined as

$$D3(r) = D3_{LLL}(r) + D3_{LTT}(r) = \langle \delta u_L(\mathbf{s}, \mathbf{r}, t) [\delta u_L^2(\mathbf{s}, \mathbf{r}, t) + \delta u_T^2(\mathbf{s}, \mathbf{r}, t)] \rangle. \quad (6)$$

$D3(r)$  is related to azimuthally averaged 2D cross-scale KE transfers  $F(k)$  through the following relationship (i.e., a Hankel transform):

$$D3(r) = -4r \int_0^\infty \frac{1}{k} F(k) J_2(kr) dk, \quad (7)$$

where  $J_2$  is the second-order Bessel function (Xie and Bühler 2019).  $F(k) > 0$  indicates a forward transfer (i.e., KE transfer toward smaller scales); conversely,  $F(k) < 0$  indicates an inverse transfer (toward larger scales). Under the assumptions of periodicity, isotropy, and homogeneity, the spectral transfers are obtained from the KE equation as (e.g., Ajayi et al. 2021; Capet et al. 2008; Dong et al. 2020):

$$F_\Pi(k) = - \int_k^{k_{max}} \text{Re} [\widehat{\mathbf{u}}^* \cdot \widehat{(\mathbf{u} \cdot \nabla \mathbf{u})}] dk, \quad (8)$$

152 where  $\widehat{(\cdot)}$  indicates Fourier transform,  $\widehat{(\cdot)}^*$  is the complex conjugate, and  $\nabla = (\partial_x, \partial_y)$  is the horizontal  
153 velocity gradient operator.

154 Xie and Bühler (2019) considered an idealized, single forcing scale scenario  $k_f$  where spectral  
155 transfer:

$$F(k) = -\epsilon_u + \epsilon H(k - k_f), \quad (9)$$

156 where  $\epsilon_u > 0$  is the upscale energy transfer (i.e., upscale KE injection rate),  $\epsilon = \epsilon_u + \epsilon_d$  is the total  
157 energy input rate ( $\epsilon_d > 0$  represents the downscale transfer),  $H$  is the Heaviside function, and  $k_f$   
158 is the forcing scale. This form captures bidirectional energy transfers and assumes that dissipation  
159 occurs at  $k \rightarrow 0$  and  $k \rightarrow \infty$  (see Fig. 1 in Xie and Bühler 2019, for possible shapes (9) can  
160 resolve).

161 The generalized expression of  $F(k)$  for multiple scales is (Balwada et al. 2022)

$$F(k) = -\bar{\epsilon} + \sum_{j=1}^{N_k} \xi_j H(k - k_j) dk_j, \quad (10)$$

162 where  $\bar{\epsilon}$  is the KE transfer rate at wavenumbers  $k < k_1$ ,  $\xi_j$  is the KE injection density (i.e.,  
163 KE injection rate per wavenumber) at each wavenumber  $k_j$ , and  $N_k$  is the number of chosen  
164 wavenumbers.  $\bar{\epsilon}$  complements  $\epsilon_u$  from (9), and may be positive for upscale transfer or negative for  
165 downscale transfer at  $k < k_1$ . Substituting (10) in (7) yields

$$D3(r) = 2\bar{\epsilon}r - \sum_{j=1}^{N_k} 4\frac{\xi_j}{k_j} J_1(k_j r) dk_j. \quad (11)$$

166 This equation provides the starting point for a discrete linear inverse problem, where the goal is to  
167 estimate  $\bar{\epsilon}$  and  $\xi_j$  at a selected range of  $k_j$  from an estimated  $D3(r)$ . By accommodating multiple  
168 forcing scales  $k_j$  and allowing for a general form of  $F(k)$ , (11) overcomes the limitations of,  
169 for example, Kolmogorov's (1991) law, which applies only to inertial ranges with unidirectional  
170 transfers (see Xie and Bühler 2019, for details).

171 Balwada et al. (2022), using the generalized expression (10) of  $F(k)$ , constrained the KE injection  
172 density  $\xi_j$  at each forcing scale to be positive  $\xi_j > 0$ , so  $F(k)$  was treated as an increasing function  
173 of  $k$ . In the ocean, nonetheless, KE can be injected and/or lost at different scales, breaking the

assumption of only positive injection made by Balwada et al. (2022). Here, we relax this assumption and allow for the energy injection density at each  $k_j$  to take either sign:  $\xi_j > 0$  indicates local KE injection (divergence of KE transfer  $F(k)$ ) at  $k_j$ , and  $\xi_j < 0$  indicates energy sink (convergence), so spectral transfers  $F(k)$  have no specific behavior.

The following section describes the inverse problem and the RLS fitting employed to estimate the KE injections and the spectral flux.

### 3. Regularized Least Squares

We use a least-squares approach to solve the linear problem, writing (11) as a matrix equation:

$$\mathbf{y} = \mathbf{H}\mathbf{x} + \mathbf{e}, \quad (12)$$

where  $\mathbf{x}$  is the column vector of size  $M \times 1$  (where  $M = N_k + 1$ ) representing the unknown parameters ( $\bar{\epsilon}$  and  $\xi_j$ ),  $\mathbf{y}$  is the vector of data to fit (i.e.,  $D3(r)$ ) of size  $N_r \times 1$  ( $N(r)$  is the number of discrete  $r$  bins),  $\mathbf{e}$  is the residual, and  $\mathbf{H}$  is the model matrix formulated from (11) of size  $N_r \times M$  defined as:

$$\mathbf{H} = \begin{bmatrix} 2r_1 & -4\frac{dk}{k_1}J_1(r_1k_1) & -4\frac{dk}{k_2}J_1(r_1k_2) & -4\frac{dk}{k_3}J_1(r_1k_3) & \cdots & -4\frac{dk}{k_{N_k}}J_1(r_1k_{N_k}) \\ 2r_2 & -4\frac{dk}{k_1}J_1(r_2k_1) & -4\frac{dk}{k_2}J_1(r_2k_2) & -4\frac{dk}{k_3}J_1(r_2k_3) & \cdots & -4\frac{dk}{k_{N_k}}J_1(r_2k_{N_k}) \\ 2r_3 & -4\frac{dk}{k_1}J_1(r_3k_1) & -4\frac{dk}{k_2}J_1(r_3k_2) & -4\frac{dk}{k_3}J_1(r_3k_3) & \cdots & -4\frac{dk}{k_{N_k}}J_1(r_3k_{N_k}) \\ \vdots & \vdots & \vdots & \vdots & \ddots & \vdots \\ 2r_{N_r} & -4\frac{dk}{k_1}J_1(r_{N_r}k_1) & -4\frac{dk}{k_2}J_1(r_{N_r}k_2) & -4\frac{dk}{k_3}J_1(r_{N_r}k_3) & \cdots & -4\frac{dk}{k_{N_k}}J_1(r_{N_r}k_{N_k}) \end{bmatrix}, \quad (13)$$

where  $k_{N_k}$  is the Nyquist wavenumber,  $r_{N_r}$  is the largest separation scale resolved, and  $dk_j$  is the wavenumber spacing.

The ordinary least-squares method is ill-suited for inverting (11) since the method can overfit data as the size of the fitted parameters is unconstrained when minimizing the mean square error  $\mathbf{e}^2 = \|\mathbf{H}\mathbf{x} - \mathbf{y}\|_2^2$ , even when weighted using the data's prior uncertainty. Consequently, ordinary least-squares methods tend to capture all the variability at the resolved scales rather than the broader patterns, producing non-physical KE injections and transfers with limited physical insight (see Supplementary Information F.2 in Balwada et al. 2022). To overcome this limitation, Balwada et al. (2022) constrained their least-squares method by assuming that energy injection rates  $\xi_j$  were

always non-negative, which is equivalent to assuming that  $F(k)$  is purely an increasing function of  $k$ .

RLS fitting i) permits the identification of convergence of KE transfers ( $\xi_j < 0$ ), ii) assumes no specific direction of the spectral flux ( $F(k)$ ), and iii) propagates the uncertainty of the fitted parameters  $\xi_j$  and  $\bar{\epsilon}$  and data  $D3(r)$  to the calculated spectra flux  $F(k)$ . An advantage of RLS is that it reduces overfitting (with some bias in our estimated parameters) by choosing a constraint with prior knowledge of the expected values. Additionally, RLS fitting is applicable for both under-determined and over-determined systems. RLS assumes that the terms in (12),  $\mathbf{x}$  and  $\mathbf{e}$  (thus, the samples of  $D3(r)$ ), have Gaussian distributions. This assumption does not preclude the use of RLS when errors deviate from Gaussianity, as the solution remains unchanged, though the posterior uncertainty estimates may no longer be appropriate. Accounting for non-Gaussian error distributions would require an alternative to RLS, which, to our knowledge, remains to be explored.

If these distributions are Gaussian, then following Kachelein et al. (2022) and Wunsch (1996), the most probable model solution is given by

$$\tilde{\mathbf{x}} = (\mathbf{H}^T \mathbf{W}^{-1} \mathbf{H} + \mathbf{P}^{-1})^{-1} \mathbf{H}^T \mathbf{W}^{-1} \mathbf{y}, \quad (14)$$

where  $\mathbf{W} = \langle \mathbf{e} \mathbf{e}^T \rangle$  is the data covariance matrix representing the prior data uncertainty and is of size  $N_r \times N_r$ ;  $\mathbf{P} = \langle \mathbf{x} \mathbf{x}^T \rangle$  is the covariance matrix representing the prior uncertainty of the fitted parameters and is  $M \times M$  (Kachelein et al. 2022; Wunsch 1996). In our work, as a practical convenience,  $\mathbf{W}$  and  $\mathbf{P}$  are defined to be diagonal matrices with off-diagonal entries of zero and with the diagonals set to the squared uncertainty of  $D3(r)$  and  $\bar{\epsilon}$ , and  $\xi_j$ , respectively. We can recover the ordinary least-squares solution in (14) by setting the elements on the diagonal of  $\mathbf{W}$  to 1 and letting  $\mathbf{P}^{-1} \rightarrow 0$ . The addition of  $\mathbf{P}$  in (14) constrains the size of the solution  $\mathbf{x}$ , preventing it from straying too far from our prior knowledge. This allows for unique solutions even when  $\mathbf{H}$  is rank deficient.

We can gain knowledge of the statistics of the differences between the expected true and estimated parameters from the posterior uncertainty covariance matrix

$$\mathbf{C}_{\mathbf{xx}} = \left\langle (\mathbf{x} - \tilde{\mathbf{x}})(\mathbf{x} - \tilde{\mathbf{x}})^T \right\rangle = (\mathbf{H}^T \mathbf{W}^{-1} \mathbf{H} + \mathbf{P}^{-1})^{-1}, \quad (15)$$

where the diagonal of (15) represents the squared uncertainty of  $\bar{\epsilon}$ , and  $\xi_j$ . The ridge regression equation presented by Wunsch (1996) is analogous to (14). We propagate the uncertainty in  $\xi_j$  and  $\bar{\epsilon}$  in (15) to uncertainty in transfers  $F(k)$  as

$$\mathbf{F}_{\mathbf{xx}} = \left\langle (\mathbf{G}\mathbf{x})(\mathbf{G}\mathbf{x})^T \right\rangle = \mathbf{G}\mathbf{C}_{\mathbf{xx}}\mathbf{G}^T, \quad (16)$$

where  $\mathbf{G}$  is the  $N_k \times M$  transformation matrix formulated with (10):

$$\mathbf{G} = \begin{bmatrix} -1 & H(k_1 - k_1)dk & H(k_1 - k_2)dk & H(k_1 - k_3)dk & \cdots & H(k_1 - k_{N_k})dk \\ -1 & H(k_2 - k_1)dk & H(k_2 - k_2)dk & H(k_2 - k_3)dk & \cdots & H(k_2 - k_{N_k})dk \\ -1 & H(k_3 - k_1)dk & H(k_3 - k_2)dk & H(k_3 - k_3)dk & \cdots & H(k_3 - k_{N_k})dk \\ \vdots & \vdots & \vdots & \vdots & \ddots & \vdots \\ -1 & H(k_{N_k} - k_1)dk & H(k_{N_k} - k_2)dk & H(k_{N_k} - k_3)dk & \cdots & H(k_{N_k} - k_{N_k})dk \end{bmatrix}. \quad (17)$$

The diagonal of  $\mathbf{F}_{\mathbf{xx}}$  (16) represents the squared uncertainty of  $F(k)$ , whereas the off-diagonal elements represent correlated uncertainty.

## 4. Datasets and Methodological Details

In this study, we show that the RLS technique is capable of estimating the shape and magnitude of the KE transfers by applying it to a two-layer QG model output where the dynamics and energetics are known. After demonstrating the utility of the improved methodology, we apply it to drifter observations from two targeted experiments in the Gulf of Mexico. These two datasets and the steps taken to estimate the structure functions are described in this section.

### 1) TWO-LAYER QG MODEL

An eddy-rich horizontal velocity field  $(u, v)$  was simulated using a two-layer QG model (PyQG; Abernathey et al. 2022) (see details in Appendix A) to test whether the RLS methodology can quantify all the details of the spectral transfers.

The model configuration is similar to the high-resolution eddy configuration of Ross et al. (2023), which generates an eddy field (Fig. 1). The configuration is a flat-bottom doubly periodic square domain of size  $L_x = L_y = 1000$  km, with  $n_x = n_y = 256$  corresponding to a uniform grid spacing

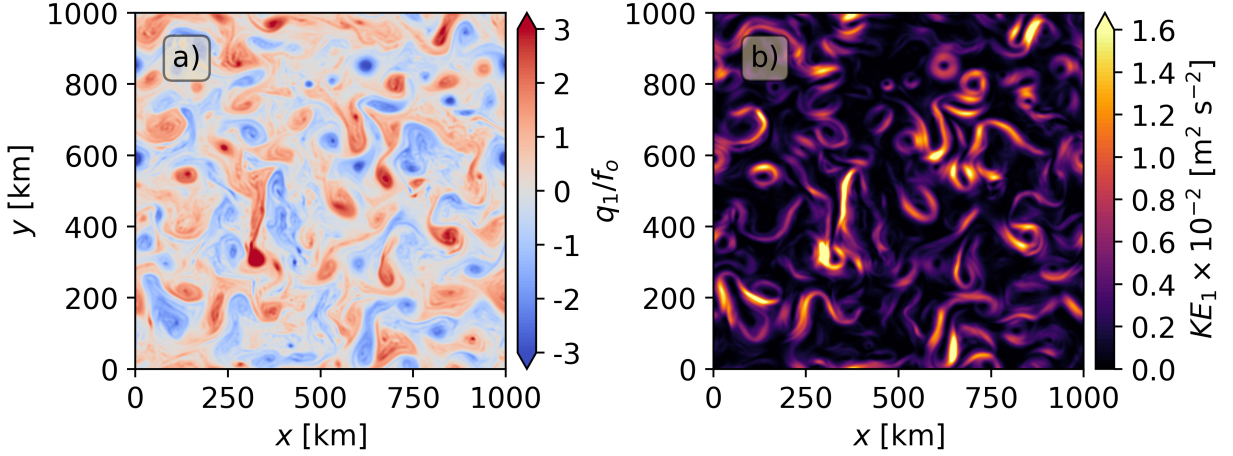


FIG. 1. Upper-layer (a) Coriolis-normalized QG potential vorticity  $q_1/f_0$  and (b)  $KE$  [ $\text{m}^2 \text{s}^{-2}$ ] from the two-layer QG model output for  $t = 6$  year.

of  $\Delta x = \Delta y \sim 3.9$  km. The simulation is forced with a mean vertical shear, set by  $U_1 = 0.025$  m  $\text{s}^{-1}$  and  $U_2 = 0$  in the top and bottom layer of mean thicknesses  $H_1 = 500$  m and  $H_2 = 2000$  m. Layer densities are chosen such that the Rossby radius  $r_d = 15$  km (characteristic of high-latitude environments), which is large enough to be well resolved on the chosen grid. Also,  $\beta = 1.5 \times 10^{-11}$   $\text{m}^{-1} \text{s}^{-1}$ , and bottom drag is  $r_{ek} = 5.787 \times 10^{-7}$   $\text{s}^{-1}$ . The model is spun up for five years and run for an additional 15 years with a time step of 1 hr. For computational convenience, we save and use daily averaged horizontal velocity fields. Since a QG model only simulates the slow dynamics, the impact of this averaging is minimal. We only compute structure functions and spectral quantities for the upper layer.

Velocity differences  $\delta \mathbf{u}$  are calculated for all unique grid-point pairs using (1) for each daily step. These velocity differences are then rotated to form longitudinal  $\delta u_L$  and transverse  $\delta u_T$  components via (2), which are then binned into equally spaced  $r$  bins spanning between 1 km and 300 km with an average increment of  $dr \sim 3.9$  km (i.e.,  $\sim \Delta x$ ). Also, since we assume isotropy, we only keep track of pair separation and not the pair orientation. These data from binned pairs form the samples/random variables, whose moments can be calculated to obtain the structure functions at different orders. To estimate the spectral fluxes via (8), and using the RLS fits with (11) and (14), the wavenumber grid is defined as  $k = 0, dk, 2dk, \dots, k_{N_y}$ , where the spacing is  $dk = 1/L_x$ , and the Nyquist wavenumber is  $k_{N_y} = 1/(2\Delta x)$ .

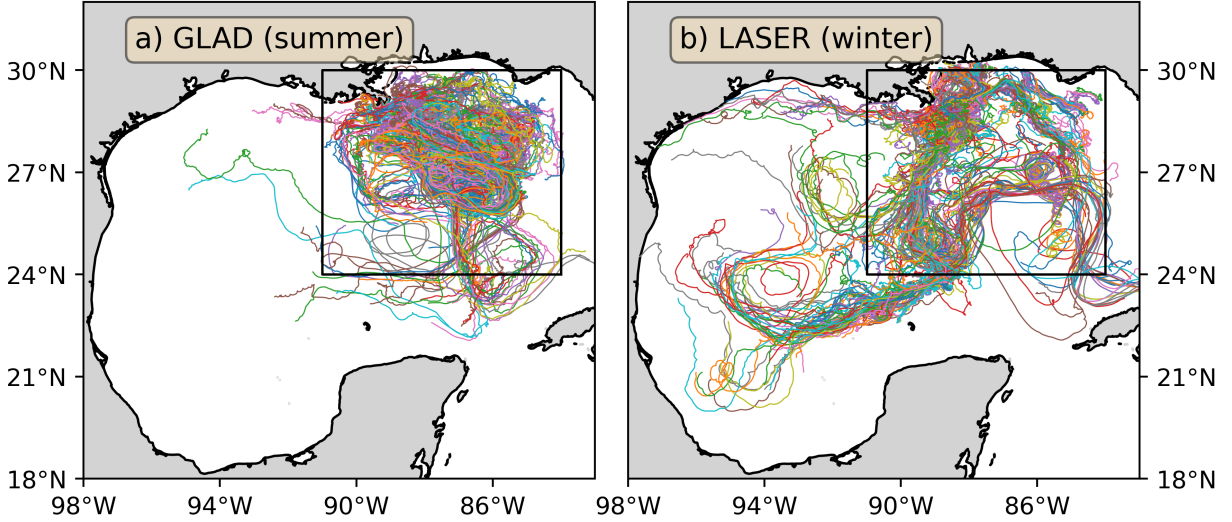


FIG. 2. Drifter trajectories from the (a) GLAD (summer) and (b) LASER (winter) experiments. Each color represents a drifter trajectory. In each panel, the box shows the subset of data used in this analysis and by Balwada et al. (2022).

## 2) DRIFTER DATA

We use data from two targeted drifter releases in the northeastern Gulf of Mexico, also used by Balwada et al. (2022). The Grand Lagrangian Deployment (GLAD) experiment released 300 drifters during summer (July-September 2012), and the Lagrangian Submesoscale Experiment (LASER) released approximately 1000 drifters during winter (January-March 2015). These GPS-tracked drifters reported positions at 5-min intervals (position error  $< 10$  m), which are subsequently low-pass filtered with a 1-hour cutoff and sub-sampled to 15 min. Following Balwada et al. (2022), we use a subset of the drifter dataset in waters deeper than 500 m (Fig. 2, box).

To calculate structure functions for this drifter data, we follow Balwada et al. (2022). First, velocity differences are calculated for all possible unique pairs of drifters at every time for each drifter dataset following (1). These velocity differences are then decomposed into  $\delta u_L$  and  $\delta u_T$  via (2) and binned into  $r$  bins for all orientations, collecting pairs of overall time sampled by each experiment. Here, the  $r$  bins were defined to be logarithmically distributed for  $10^1 \text{ m} \leq r \leq 10^6 \text{ m}$  as  $r_a = r_0 \times 1.5^a$ , where  $r_0 = 10 \text{ m}$  and  $a = (0, 1, 2, 3, \dots)$  as we expect that flow length scales increase with separation distance. Using linearly spaced bins reduces the number of pairs per bin by two orders of magnitude and produces similar, but noisier, third-order structure function estimates

compared to those obtained with log-spaced bins (not shown). These data from binned pairs form the samples/random variables, whose raw moments can be calculated to obtain the structure functions at different orders. We set up the wavenumbers  $k_j$  linearly with spacing  $dk_j = 1/\max(r)$ , and the Nyquist wavenumber is  $k_{N_y} = 1/[2(r_2 - r_1)]$ . This results in the model matrix  $\mathbf{H}$  having more unknowns than data points (i.e.,  $M > N_r$ ). Both RLS and NNLS are well-suited for such underdetermined problems.

## 5. Results

Here, we present the results of applying RLS to the velocity fields from the QG simulation, followed by its application to drifter observations in the Gulf of Mexico. We also thoroughly discuss how uncertainties may be estimated, and we compare RLS-derived results against other approaches when possible.

### *a. Two-Layer Quasi-Geostrophic Turbulence*

#### 1) TURBULENCE PHENOMENOLOGY AND KE TRANSFERS

The phenomenology of two-layer QG turbulence is more complex than 2D turbulence, but some qualitatively similar features arise (Vallis 2017). The five-year upper-layer isotropic energy spectrum  $E(k)$  is calculated by Fourier transforming the daily-averaged horizontal velocity fields  $(u, v)$  with no detrending or windowing. The 95% confidence intervals are estimated using the  $\chi^2$  distribution and setting the degrees of freedom as the ratio of the length of the time series and its integral time scale (i.e., first zero-crossing in the autocorrelation function).  $E(k)$  follows a power law of approximately  $k^{-4}$  at higher wavenumbers (blue solid, Fig. 3a), which indicates forward enstrophy cascade. Results based on the last month of hourly-averaged model output (green solid; Fig. 3a) are statistically indistinguishable from the five-year average, showing the minimum impact of using daily averaged fields instead of hourly. While the energy spectra are useful diagnostics, by themselves, they provide limited information about the detailed properties of the energy transfers.

In two-layer QG flows, the flow is stirred, or energy is injected into the flow, by baroclinic instability. Similar to 2D turbulence, we expect there to be an inverse transfer of energy (and a forward transfer of enstrophy) in each layer, and a small forward transfer at high wavenumbers en route to small-scale dissipation. At the largest scales resolved, the flow becomes barotropic, and

thus some of the energy cascading to larger scales in the top layer is transferred to the lower layer. To confirm this phenomenology, we diagnose the spectral flux  $F_{\Pi}(k)$  from our QG simulation, calculated as the five-year average of the daily spectral flux computed directly in spectral space using (8) and the daily  $u, v$  fields. This long-time average ensures a close-to-perfect estimate of the equilibrium spectral flux. Since the domain is doubly periodic, no detrending or windowing was applied (as done for estimating  $E(k)$ ), and horizontal velocity gradients  $\nabla \mathbf{u}$  are estimated in spectral space. In practice,  $F_{\Pi}(k)$  is computed in two steps: first, the contributions of all Fourier modes within a small wavenumber bin centered at each target wavenumber  $k_j$  (i.e., over the interval  $k_j - dk/2 - k_j + dk/2$ ) are summed; these binned sums represent the kinetic energy injections  $\xi_j$  at that scale  $k_j$ . Second, the spectral flux  $F_{\Pi}(k)$  is obtained by integrating (cumulative summing) these injections from  $k_{min}$  up to the maximum wavenumber  $k_{Ny}$ , providing a discrete approximation of the continuous integral in (8).

The KE injections and spectral fluxes for the top layer corroborate the theoretical picture: (i) energy is injected ( $\xi_j > 0$ ) into the flow at  $k \sim 10^{-2}$  cycles  $\text{km}^{-1}$  (Fig. 3b), (ii) energy is lost ( $\xi_j < 0$ ) from the top layer flow at scales  $k < 8 \times 10^{-3}$  cycles  $\text{km}^{-1}$  (Fig. 3b), and (iii) the energy flux is upscale (inverse) across most scales (Fig. 3c), with a transition to a downscale (forward) transfer at  $k > 0.02$  cycles  $\text{km}^{-1}$  en route to dissipation (small inset, Fig. 3c). Our goal in this section is to estimate the spectral flux expected in QG turbulence (Fig. 3b,c) using the third-order structure function framework (11) (Xie and Bühler 2019; Balwada et al. 2022) and RLS (14) (Wunsch 1996; Kachelein et al. 2022). We further demonstrate that RLS outperforms NNLS by capturing the full structure of energy injections and transfers, including both positive and negative contributions at each wavenumber.

## 2) SAMPLES AND UNCERTAINTY OF THIRD-ORDER STRUCTURE FUNCTION

An important assumption for RLS to be optimal is that the prior errors  $\mathbf{e}$  are Gaussian-distributed (Wunsch 1996; Kachelein et al. 2022). In this subsection, we examine the distribution of the pair samples of  $D3(r)$  to determine if the errors in  $D3(r)$  are Gaussian distributed.

The third-order structure function  $D3(r)$  is an ensemble mean of  $\delta u3(\mathbf{s}, \mathbf{r}, t) = \delta u_L(\mathbf{s}, \mathbf{r}, t)[\delta u_L^2(\mathbf{s}, \mathbf{r}, t) + \delta u_T^2(\mathbf{s}, \mathbf{r}, t)]$  over many pair samples coming from different locations, orientations, and times. The distribution of the pair samples  $\delta u3(\mathbf{s}, \mathbf{r}, t)$  is shown as a function of

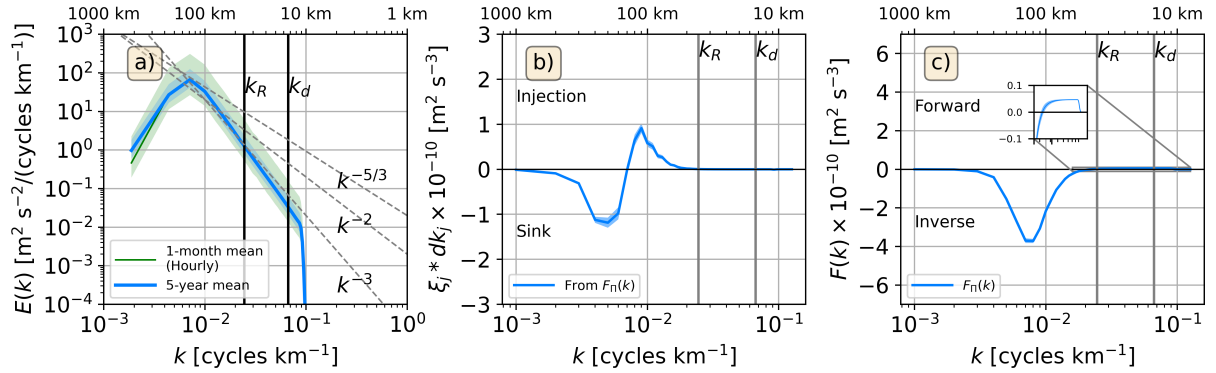


FIG. 3. Five-year mean isotropic KE (a) spectra  $E(k)$  [ $\text{m}^2 \text{s}^{-2} / (\text{cycles km}^{-1})$ ], (b) injection density per wavenumber spacing  $\xi_j * dk_j$  [ $\text{m}^2 \text{s}^{-3}$ ], and (c) transfers  $F_{\Pi}(k)$  estimated using (8) [ $\text{m}^2 \text{s}^{-3}$ ] (blue solid line). Power laws (gray dashed lines) are shown in (a). Green solid line in (a) is the mean  $E(k)$  estimated from one month of hourly averaged model outputs. Shaded areas in (a) show the  $\chi^2$  95% confidence intervals. Positive  $\xi_j * dk_j$  in (b) indicates KE injection.  $k_R$  and  $k_d$  are the model's Rhines and Rossby deformation wavenumbers (vertical gray solid line), respectively. Small inset in (c) zooms in on the highest wavenumbers resolved, showing a forward transfer. Positive  $F(k)$  in (c) indicates forward KE transfer.

time at two different separations ( $\sim 44$  and  $\sim 83$  km) in Fig. 4. For convenience, we only show the first 200 days of the five years; given the setup, the properties of the simulation do not change over time. As expected in turbulent regimes (Barndorff-Nielsen et al. 2004), the  $\delta u_3$  distributions are non-Gaussian, exhibiting heavy tails and slight skewness, and vary over time, with intermittent events reaching between 10 and 35 standard deviations from the mean. These extreme events play a role in setting the mean, and thus  $D3(r)$ . We conclude that the pair samples of the third-order structure function are non-Gaussian distributed. Consequently, we look for an alternative avenue to generate Gaussian-distributed samples and errors in  $D3(r)$ .

To generate Gaussian-distributed samples, we average the pair samples  $\delta u_3(\mathbf{s}, \mathbf{r}, t)$  over the full spatial domain and all orientations of  $\mathbf{r}$  ( $\overline{\delta u_3}$ ), and without any temporal average. Note that this average is meant to be an approximation to the ensemble average ( $\langle \cdot \rangle$ ) of (6). These samples are denoted by  $\overline{\delta u_3}(r, t)$ . Averaging  $\delta u_3(\mathbf{s}, \mathbf{r}, t)$  over all orientations and positions results in approximately Gaussian-distributed sample means  $\overline{\delta u_3}(r, t)$  at each  $r$  per the central limit theorem (Stroock 2010). To confirm that  $\overline{\delta u_3}(r, t)$  is Gaussian distributed, we show PDFs of  $\overline{\delta u_3}(r, t)$  normalized by the standard deviation of the sample means  $\sigma_{\overline{\delta u_3}}$  at two separations as examples

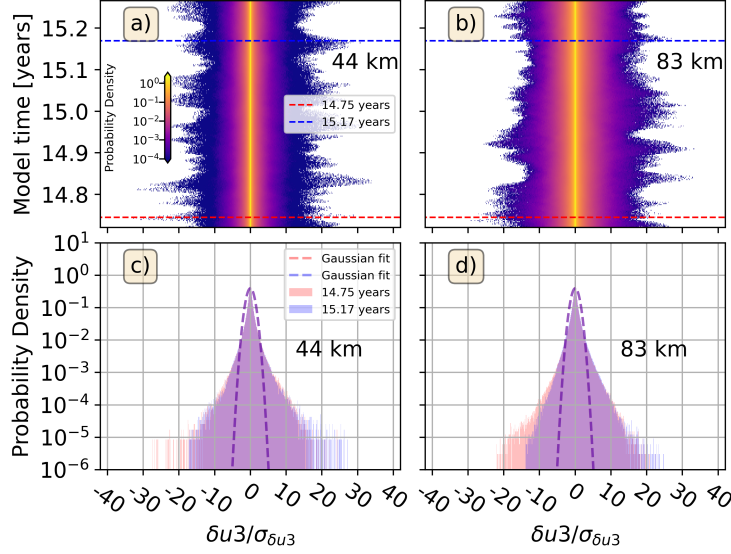


FIG. 4. (a)-(b) Hovmöller diagram of the probability density (log<sub>10</sub> scale) of the daily standard-deviation-normalized pair samples of third-order structure function  $\delta u3/\sigma_{\delta u3}$  for the (a) 44-km and (b) 83-km  $r$  bin. Dashed red and blue lines indicate the 14.75 and 15.17 model years. (c)-(d) Probability density (in log<sub>10</sub> scale) of  $\delta u3/\sigma_{\delta u3}$  for the (c) 44-km and (d) 83-km  $r$  bin. Red and blue bars are the 14.75- and 15.17-year PDFs, respectively. Dashed curves show the Gaussian fit calculated from the mean  $\delta u3(\mathbf{s}, \mathbf{r}, t)$  and standard deviation  $\sigma_{\delta u3}$ , respectively.

(Fig. 5a). Visually, these PDFs show that the distribution of sample means is close to Gaussian, confirmed by good agreement with the expected Gaussian distribution (dashed), and have non-zero means. In contrast to the pair samples  $\delta u3(\mathbf{s}, \mathbf{r}, t)$  (Fig. 4), the means and tails of  $\overline{\delta u3}(r, t)$  fall within three to four standard deviations (Fig. 5a). Also, the estimated skewness and excess kurtosis at each  $r$  indicate that samples are lightly positively skewed, with excess kurtosis  $< 1$  (with moderate tails) (Fig. 5b). Thus, the  $\overline{\delta u3}(r, t)$  is approximately Gaussian distributed and satisfies the RLS assumption of Gaussian-distributed errors.

### 3) REGULARIZED LEAST-SQUARES FITTING AND KE TRANSFERS

Here we proceed with the inversion problem using RLS, to test whether a trustworthy estimate of  $F(k)$  can be recovered from a given  $D3(r)$ . The five-year averaged  $D3(r)$  is estimated here by time averaging  $\overline{\delta u3}(r, t)$ . We note that averaged samples  $\overline{\delta u3}(r, t)$  (orange solid, Fig. 6a) are qualitatively similar to the five-year mean  $D3(r)$  (thick black solid, Fig. 6a).  $D3(r)$  for the

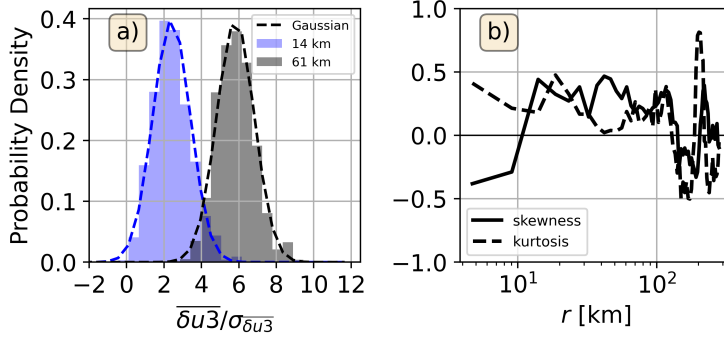


FIG. 5. (a) Probability density of standard-deviation-normalized daily averaged samples  $\overline{\delta u 3} / \sigma_{\overline{\delta u 3}}$  for 14 km (gray) and 61 km (blue) bins calculated using five-year daily averages. Dashed lines show the Gaussian fit. (b) Skewness (solid line) and excess kurtosis (dashed line) as a function of  $r$  bin. For a Gaussian distribution, skewness and excess kurtosis are both zero.

upper-layer is positive for  $r < 100$  km, with a maximum at  $r \sim 70$  km, which qualitatively suggests an inverse cascade based on its sign. However, at  $r > 100$  km,  $D3(r)$  takes on a negative value, even though the spectral transfer  $F_{\Pi}(k)$  exhibits no indication of a forward cascade at these scales (blue solid, Fig. 6c). This negative lobe in  $D3(r)$  is a result of the Bessel function in (7), and stands as a cautionary example of situations when the sign of  $D3(r)$  is a misleading indicator of the energy transfer directionality. Thus, it is beneficial to estimate  $F(k)$  by inverting (11) rather than relying on the sign of  $D3(r)$ .

Apart from the assumptions of Gaussianity inherent to RLS, the structure-function framework described in Section 2 also requires that the flow be homogeneous over the spatial and temporal domain being considered and that the mean flow have no gradients. Since we generated data from a periodic simulation with a prescribed constant background flow, both these assumptions are satisfied by construction (also visually apparent in Fig. 1). However, it should be noted that if we only observed the system over short periods, it would be hard to assess whether the background mean is zero or not, just from the data (see Appendix C). Since the assumptions of the structure-function framework and the RLS approach are satisfied in this context, we proceed to set up the RLS problem. This involves constructing the matrices for the prior data uncertainty  $\mathbf{W}$  and the prior uncertainty of the fitted parameters  $\mathbf{P}$ .

The prior uncertainty of  $D3(r)$  is estimated by calculating the standard error, i.e., the standard deviation of the daily averaged samples  $(\overline{\delta u 3}(r, t))$ ; orange solid, Fig. 5a) divided by the square

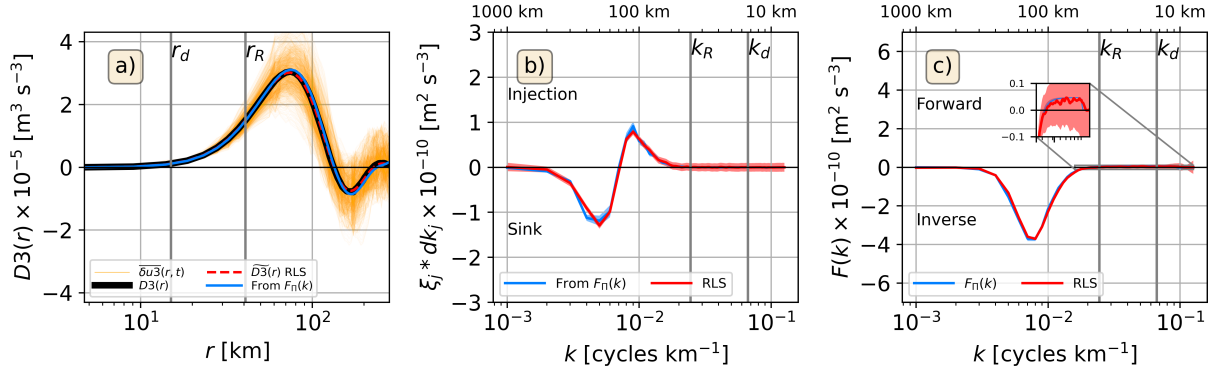


FIG. 6. (a) Third-order structure function  $D3(r) [\text{m}^3 \text{s}^{-3}]$  for the model's upper layer (black thick solid line). Daily  $\overline{\delta u^3}(r, t)$  (pair samples averaged for all positions and orientations) are shown in orange solid lines. RLS-fitted structure function  $\widehat{D3}(r)$  is shown in thin dashed red line.  $D3(r)$  estimated via (7) using the KE transfers calculated using the spectral method  $F_{\Pi}(k)$  from (8) is shown in blue solid line. Solid vertical line shows the model's Rossby baroclinic radius  $r_d$  and Rhine's scale  $r_R$ . (b) KE injection  $\xi_j * dk_j$  (divergence of KE transfers)  $[\text{m}^2 \text{s}^{-3}]$ . Positive values indicate KE injection (divergence). (c) Cross-scale KE transfers  $F(k) [\text{m}^2 \text{s}^{-3}]$ . Positive and negative transfers indicate a forward (downscale) and inverse (upscale) KE transfer. Red and blue solid lines in (b-c) are the RLS-based and spectral estimates (derived from (8)). Shaded red in (c-d) are the posterior uncertainty in the injections (15;  $\text{diag}(\sqrt{\mathbf{C}_{xx}})$ ) and transfers (16;  $\text{diag}(\sqrt{\mathbf{F}_{xx}})$ ). The standard error of the spectral-based estimates is represented by the blue shading. Vertical gray solid lines in (c)-(d) show the model's Rhines wavenumber  $k_R$  and Rossby wavenumber  $k_d$ . Small inset in (c) zooms in on the highest wavenumbers.

root of the degrees of freedom  $\sqrt{N(r)}$  (see Appendix B for details). Here, the degrees of freedom are not simply the number of days, since  $\overline{\delta u^3}(r, t)$  is not an independent sample each day. To estimate  $N(r)$ , we first calculate the scale-dependent decorrelation time scale  $T_{scale}(r)$  following Balwada et al. (2022) via (B1) (black solid, Fig. B1a). Subsequently, the scale-dependent degrees of freedom  $N(r)$  are computed using  $T_{scale}(r)$  and the total number of days from (B2) (red solid, Fig. B1b). We use the square of the standard errors in  $D3(r)$  as the diagonal of  $\mathbf{W}$ ; the off-diagonal elements are set to zero.

There is no physical guidance on how to set prior uncertainty for the parameters to be estimated, so we construct  $\mathbf{P}$  with the help of a heuristic approach called the “trade-off curve” method (Hansen 1999). The prior uncertainty is chosen to maximize the fit to the data ( $D3(r)$ ) while keeping the size of the fitted parameters  $\xi_j$  small. This “sweet spot” is determined by estimating a trade-off

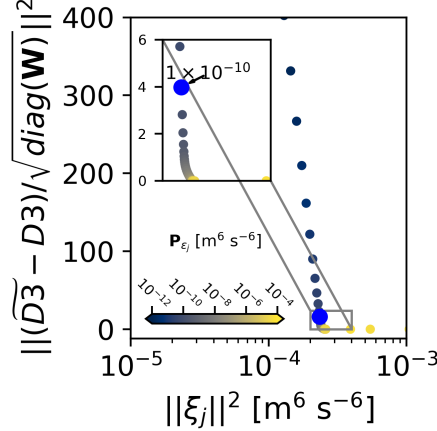


FIG. 7. Trade-off L-curve for different squared uncertainties employed for  $\mathbf{P}_{\xi_j}$  (color bar). The x-axis shows the L2 norm of the fitted parameters  $\xi_j$  [ $\text{m}^6 \text{s}^{-6}$ ]. The L2 norm of the residuals normalized by the uncertainty of  $D3(r)$  is shown on the y-axis. Small inset shows where the fitted structure function  $\widetilde{D3}(r)$  resembles the calculated  $D3(r)$ . Optimal value  $\mathbf{P}_{\xi_j} = 1 \times 10^{-10} \text{ m}^6 \text{s}^{-6}$  used in this study is shown (blue dot).

between the L2 norm of the estimated  $\xi_j$  and the L2 norm of the model-data misfit normalized by the prior uncertainty in  $D3(r)$ . This heuristic approach is a way to avoid overfitting.

Choosing a larger prior uncertainty for  $\xi_j$  slightly reduces the misfit but increases the size of  $\xi_j$  (overfits) and the posterior uncertainty. Conversely, the data-model misfit increases as the prior uncertainty decreases (over-smoothed solution). Using this method, the  $\mathbf{P}$  diagonal's first element is selected as  $10^{-7} \text{ m}^4 \text{s}^{-6}$  corresponding to the squared prior uncertainty in  $\bar{\epsilon}$ . Changing the squared uncertainty in  $\bar{\epsilon}$  by two orders of magnitude does not alter the shape of the trade-off curve (not shown). For the prior uncertainty in  $\xi_j$  (remaining diagonal entries), we set the optimal value to  $1 \times 10^{-10} \text{ m}^6 \text{s}^{-6}$  for all resolved wavenumbers (blue dot, Fig. 7).

With these parameter choices, we perform a fit to  $D3(r)$  (thick black solid, Fig. 6a) to test our RLS approach. KE injections are estimated directly by fitting  $D3(r)$  using (11) and (14), as they are the unknowns  $\mathbf{x}$ . Subsequently, energy transfers  $F(k)$  are calculated using (10). The RLS-based energy injections  $\xi_j$  (red solid, Fig. 6b) match both the positive and negative energy injections (blue solid, Fig. 6b). The RLS  $F(k)$  (red solid, Fig. 6c) indicates the presence of an inverse transfer at almost all  $k_j$  and a forward transfer for  $k > 0.02 \text{ cycles km}^{-1}$  similar to the spectral transfer  $F_{\Pi}(k)$  (blue solid, Fig. 6c, inset). The RLS-based structure function  $\widetilde{D3}(r)$ , obtained by multiplying the

model matrix  $\mathbf{H}$  with the fitted parameters  $\tilde{\mathbf{x}}$  (red dashed, Fig. 6a), overlaps with the calculated  $D3(r)$  (thick black solid, Fig. 6a) due to the small residual of the fit. Both curves agree well with the theoretical  $D3(r)$  (blue solid, Fig. 6a), which is derived from  $F_{\Pi}(k)$  (blue solid, Fig. 6c) via (7).

#### 4) COMPARING RLS TO OTHER ESTIMATION APPROACHES

We now test whether NNLS fits (used by Balwada et al. 2022) are capable of capturing the properties of the KE injections and transfers expected in the two-layer QG model. To estimate the NNLS-based  $\bar{\epsilon}$ ,  $\xi_j$ , and  $F(k)$ , we first estimated the fitted structure function  $\widetilde{D3}(r)$  by averaging  $\overline{\delta u^3}(r, t)$  and inverted it using NNLS. The fitted structure function  $\widetilde{D3}(r)$  is calculated as  $\mathbf{H}\tilde{\mathbf{x}}$ . To calculate the standard error, we inverted the daily  $\overline{\delta u^3}(r, t)$  using NNLS to generate daily estimates of  $\xi_j$ ,  $\bar{\epsilon}$ , and  $F(k)$ . The standard errors in the spectral quantities were then calculated by estimating the standard deviation divided by  $\sqrt{N}$ , where  $N$  is the degrees of freedom at the largest  $r$ ; this definition of  $N$  sets an upper bound for the standard error. As expected, the NNLS method is unable to fit  $D3(r)$  for all  $r$  (green dashed, Fig. 8). Consequently, energy injection estimates and spectral transfers are non-physical (green dashed, Fig. 8b,c). Therefore, NNLS is ill-suited for estimating convergence of  $F(k)$  (i.e.,  $\xi_j * dk_j < 0$ ).

From (7), we can expect that  $F(k)$  for  $k > 0.02$  cycles  $\text{km}^{-1}$  behaves as an increasing function of wavenumber given that  $D3(r)$  increases with  $r$  for  $r < 50$  km (blue solid, Fig. 8a). This assumption is corroborated by the shape of  $F_{\Pi}(k)$ , which is an increasing function for  $k > 8 \times 10^{-3}$  cycles  $\text{km}^{-1}$  (blue solid, Fig. 8c). Therefore, we hypothesize that NNLS could potentially capture the size and shape of the  $\xi_j$  and  $F(k)$  values for  $k > 8 \times 10^{-3}$  cycles  $\text{km}^{-1}$  (blue solid, Fig. 8b,c). A partial fit may help to recover the shape of  $F(k)$  over a partial range of scales. The partial fit and estimates and their standard errors are calculated similarly to the full  $r$  range.

The NNLS-based structure function  $\widetilde{D3}(r)$  over the partial range matches  $D3(r)$  well by eye (red dashed-dotted, Fig. 8a). Unlike the NNLS fit over the full range, the partial  $F(k)$  shows the presence of an inverse transfer (red dashed-dotted, Fig. 8c). However, the estimated energy injections take on non-zero values at the wrong scale and are a factor of two larger than the spectral injections (blue solid, Fig. 8b).

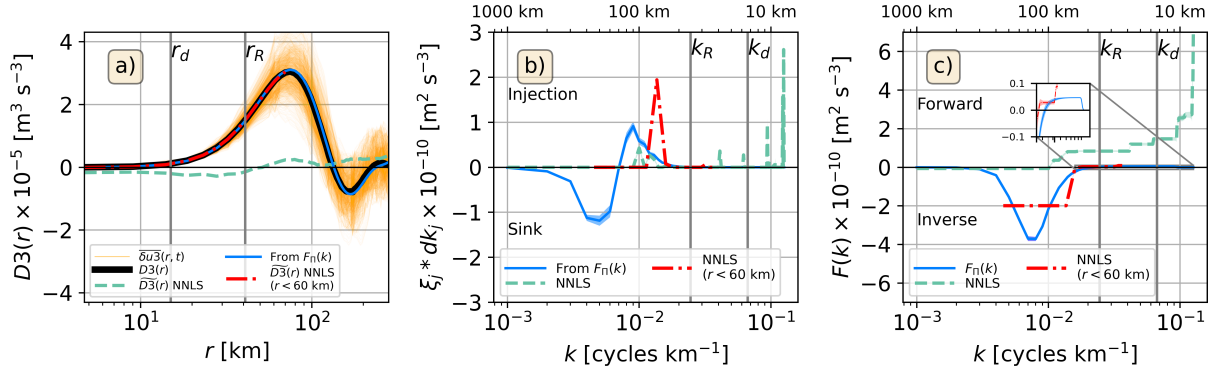


FIG. 8. (a) Third-order structure function  $D3(r)$  [ $\text{m}^3 \text{s}^{-3}$ ] for the model's upper layer (thick black solid line). Daily  $\overline{\delta u^3}(r, t)$  (samples averaged for all positions and orientations) are shown in orange solid lines.  $D3(r)$  estimated via (7) using the KE transfers calculated using the spectral method  $F_{\Pi}(k)$  from (8) is shown in blue solid line. (b) KE injection  $\xi_j * dk_j$  (divergence of KE transfers) [ $\text{m}^2 \text{s}^{-3}$ ]. Positive values indicate KE injection (divergence). (c) Cross-scale KE transfers  $F(k)$  [ $\text{m}^2 \text{s}^{-3}$ ]. Positive and negative transfers indicate a forward (downscale) and inverse (upscale) KE transfer. Green dashed and blue solid lines are the NNLS-based and spectral estimates (derived from (8)). Red dashed-dotted line is the NNLS-based estimates using  $D3(r)$  where  $r < 60$  km. Colored shading areas show the standard error of the estimated quantities. Small inset in (c) zooms in on the highest wavenumbers.

In this section, we showed that RLS can estimate the KE transfers and injections without assuming a prior shape of  $F(k)$  or sign of  $\xi_j$ . The RLS method is superior to the NNLS as it constrains the size of the fitted parameters. Also, this approach provides posterior uncertainties for  $\bar{\epsilon}$  and  $\xi_j$ , and propagates the error to estimate uncertainty in  $F(k)$ . Having established trust in the RLS approach and the  $D3(r)$  framework, we proceed in the next subsection to show the application of the improved methodology to sparse drifter data and compare the  $\xi_j$  and  $F(k)$  estimated using RLS with those estimated by Balwada et al. (2022) using NNLS.

## b. Application to sparse drifter data

### 1) PAIR-SAMPLE DISTRIBUTION OF $\delta u^3$ AND UNCERTAINTY OF $D3(r)$

For the drifter data, as for the QG model, we start by considering the distribution from the pair samples of  $\delta u^3(\mathbf{s}, \mathbf{r}, t)$  for each season, which are averaged over all orientations and positions to

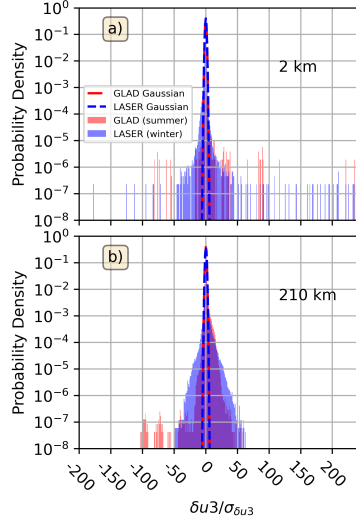


FIG. 9. PDFs of the pairwise samples of third-order structure functions, normalized by their standard deviation ( $\delta u_3 / \sigma_{\delta u_3}$ ), for the GLAD (summer; red) and LASER (winter; blue) datasets at (a)  $\sim 2$  km and (b) 210 km bins. The y-axis is shown on a logarithmic scale. Dashed lines indicate the corresponding Gaussian fits.

estimate the third-order structure function  $D3(r)$ . In contrast to the dense, gridded sampling from the QG simulations, drifters only sample  $\delta u_3(\mathbf{s}, \mathbf{r}, t)$  at sparse spatial locations ( $\mathbf{s}$ ) and orientations ( $\mathbf{r}$ ). Also, drifters tend to cluster in convergent flows and/or flows with large vorticity, resulting in biased sampling that can affect both the shape and magnitude of the third-order structure function (Pearson et al. 2020). Corrections for this effect on the first, second, and third-order structure functions have been proposed (Pearson et al. 2019). Nonetheless, Balwada et al. (2022) showed that the direction of KE transfers at  $O(1)$  km scales remains unchanged even without such corrections. We proceed with estimating  $D3(r)$  and solving the inversion problem for each dataset.

Akin to the QG model (Fig. 4), the distributions from the drifters are highly non-Gaussian, with long tails and occasional outliers as large as  $115\sigma_{\delta u_3}$  (Fig. 9), as expected for turbulent regimes (Barndorff-Nielsen et al. 2004). Since drifters do not provide a large number of pair samples at a single time, as in the QG model, we cannot simply average over positions and orientations at a single time, as the limited number of samples would produce noisy estimates. Instead, we seek an alternative method to construct Gaussian-distributed samples of  $D3(r)$  to bound the confidence intervals for each dataset.

To estimate these samples and the corresponding uncertainty, we use bootstrapping. Standard bootstrapping assumes that all data samples (pair samples of  $\delta u_3$  in this case) are independent. Using this approach would yield unrealistically small standard errors (one-to-two orders of magnitude smaller than  $D_3(r)$ ), hence small posterior  $\xi_j$ ,  $\bar{\epsilon}$ , and  $F(k)$  uncertainties (not shown). This happens because many pair samples are correlated due to proximity in space or time, which is not properly accounted for in this standard approach. To overcome this difficulty, we use moving-block bootstrapping, which allows us to estimate uncertainty when the contributing samples are correlated (Kunsch 1989).

For moving-block bootstrapping, we construct a pseudo-time series of  $\delta u_3(r, t)$  for each  $r$  bin from several concatenated time series of different pairs of drifters. The concatenated records inherently have some autocorrelation because of the spatio-temporal proximity between pairs. Then we divide the concatenated  $\delta u_3(r, t)$  data for each  $r$  bin into 50% overlapping blocks of data of size  $L(r)/N(r)$ , where  $L(r)$  is the length of the concatenated data per  $r$  bin and  $N(r)$  is the number degrees of freedom. Here,  $N(r)$  is roughly estimated by dividing the total duration of each drifter experiment by the decorrelation timescale at each  $r$ , which was calculated with the help of  $D_2(r)$  (see Appendix B; Fig. B2). Next, we sample  $b$  blocks with replacement at each  $r$  and concatenate them to construct a pseudo-time series of  $\delta u_3(r, t)$  of length  $L(r)$ . The mean of this pair-sample set gives a bootstrap estimate of  $D_3(r)$  (denoted as  $D_{3b}(r)$ ). Bootstrap estimates  $D_{3b}(r)$  are Gaussian-distributed (Stroock 2010) after repeating the procedure 2000 times. This moving-block bootstrapping contrasts with that used by Balwada et al. (2022), where the concatenated block of size  $L(r)$  was divided into  $N(r)$  blocks.

PDFs of the  $D_{3b}(r)$  for selected  $r$  bins show near-Gaussian distributions for both experiments (Fig. 10a,b). PDFs from the GLAD dataset show light positive skewness (red bars, Fig. 10a,b). The near-zero skewness and excess kurtosis for most of the  $r$  bins confirm that the bootstrapped quantities have near-Gaussian distributions (Fig. 10c,d). The two smallest  $r$  bins for the LASER experiment show large negative skewness and excess kurtosis (blue solid, Fig. 10c,d) due to the large outliers in the concatenated data. However, the RLS results are insensitive to the inclusion or removal of these two bins since  $J_1(kr)$  in (11) is small for those bins. The prior uncertainty in  $D_3(r)$  was estimated by computing the standard deviation of these bootstrapped  $D_{3b}(r)$  distributions.

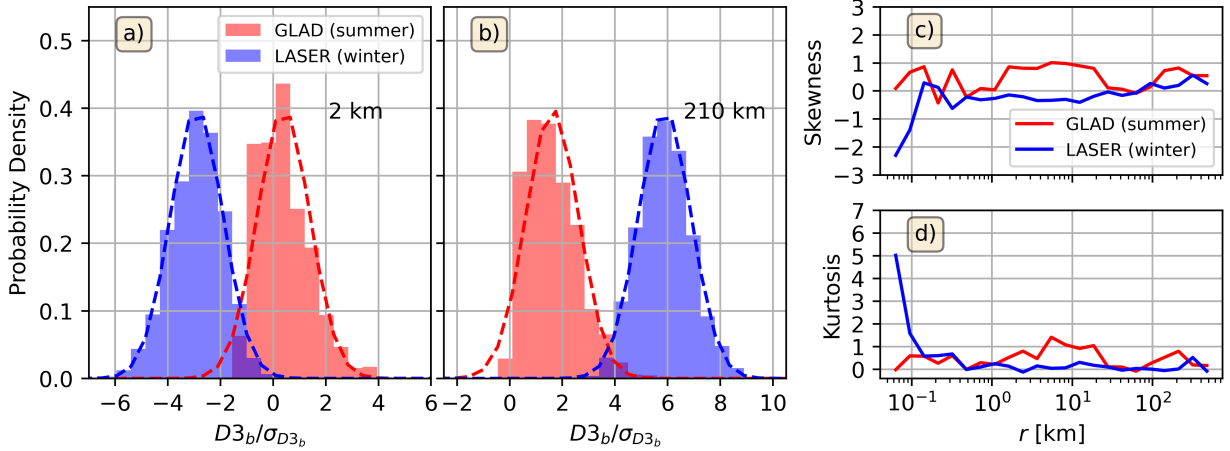


FIG. 10. (a)-(b) PDFs of standard-error-normalized bootstrapped means  $D3_b/\sigma_{D3_b}$  generated using moving-block bootstrapping for GLAD (red) and LASER (blue) experiments, respectively. Dashed lines show the Gaussian fits. Only the (a) 2 km and (b) 210 km bins are shown. (c) Skewness and (d) excess kurtosis estimated for the bootstrapped means.

## 2) KE TRANSFERS FROM SPARSE DRIFTER DATA

Next, we apply the RLS approach to deduce the seasonality of the KE transfers and injection rates by inverting (11) with the estimated  $D3(r)$  from the summertime GLAD and wintertime LASER experiments (Fig. 11a,b).  $D3(r)$  for each dataset was calculated by replacing the ensemble averaging (6) with an average of all pair samples  $\delta u_3$  per  $r$  bin, which is the same as the mean estimated from the samples generated by the modified bootstrapping approach. The summertime  $D3(r)$  could indicate that  $F(k)$  does not purely increase with  $k$  since  $D3(r)$  decreases slightly between  $10 \text{ km} \leq r \leq 60 \text{ km}$  (dark red solid; Fig. 11a), which could indicate convergence of  $F(k)$  (i.e.,  $\xi_j < 0$ ). The wintertime  $D3(r)$  qualitatively suggests the presence of bidirectional energy transfers as they transition from negative to positive values as  $r$  increases (dark blue solid, Fig. 11b); the slight decrease in  $D3(r)$  for  $r < 1 \text{ km}$  suggests a weakening of the forward transfer. We note that the first-order structure function  $D1(r)$  for both seasons shows that the condition of homogeneity is not satisfied for all  $r$  with the limited sampling (i.e.,  $D1(r) \neq 0$ ; see Appendix C, Fig. C2). We proceed with caution in interpreting our results.

To set up the RLS method, the diagonal entries of  $\mathbf{W}$  are set as the squared uncertainty in  $D3(r)$  (shaded areas, Fig. 11a,b). We set the squared uncertainty in  $\bar{\epsilon}$  to  $1 \times 10^{-7} \text{ m}^4 \text{ s}^{-6}$  (first entry of

the diagonal of  $\mathbf{P}$ ), whereas the squared prior uncertainty of  $\xi_j$  (the remaining diagonal entries) as  $4 \times 10^{-4} \text{ m}^6 \text{ s}^{-6}$  after using the “L-curve” method (not shown). To test sensitivity, we varied the squared uncertainty in  $\bar{\epsilon}$  by three orders of magnitude and found that the RLS results were unaffected. We also compared our RLS estimates with estimates derived using NNLS (Balwada et al. 2022). To estimate the uncertainty in the NNLS-based  $\xi_j$  and  $F(k)$  for each season per  $r$  bin, we invert the 2000 bootstrap means  $D3_b(r)$  to estimate 2000 bootstrapped  $\xi_j$  (11) and  $F(k)$  (10).

The RLS-based  $D3(r)$  (black solid, Fig. 11a,b) matches the observed  $D3(r)$  (dark red and blue solid, Fig. 11a,b) better than the NNLS fit (light red and blue solid, Fig. 11a,b) for both seasons. The NNLS fit (light red solid) fails to capture the slight decrease in magnitude in the GLAD  $D3(r)$  located at  $r \sim 60 \text{ km}$  (dark red solid). The RLS-based estimates of  $\xi_j$  (black solid; Fig. 11c,d) are smoother and smaller in amplitude (though also statistically not different from zero) than the NNLS estimates (light red and blue solid, Fig. 11c,d and insets). Moreover, the NNLS fit fails to estimate any negative energy injection rates by design, whereas the RLS-based  $\xi_j$  values suggest the presence of such negative injections, as seen in the summer at intermediate scales of  $k \sim 0.07 \text{ cycles km}^{-1}$  (black solid, small inset in Fig. 11c).

The spectral flux  $F(k)$  estimated using RLS (black solid, Fig. 11e,f) follow a similar shape and amplitude as those estimated using NNLS (light red and blue solid, Fig. 11e,f, respectively): a bidirectional KE transfer where an inverse transfer dominates at mesoscales and forward transfer is present at submesoscales. The transition scale from inverse to forward transfer shows a seasonal modulation. The RLS- and NNLS-based  $F(k)$  estimates are not statistically distinguishable for each season. Unlike the NNLS fits, which show  $F(k)$  to be statistically different from zero at nearly every  $k_j$  in both seasons, the RLS fits reveal that the summer forward transfer at submesoscales ( $k > 1 \text{ cycles km}^{-1}$ ) is not statistically distinguishable from zero (black solid and gray shading, Fig. 11e). These results suggest that the summertime forward transfer at submesoscales is more variable than in winter, likely reflecting the prevalence of many weaker events alongside a few strong ones (black solid and gray shading, Fig. 11f).

## 6. Summary and Discussion

We present an improved methodology to estimate cross-scale KE transfers  $F(k)$  and injection rates  $\xi_j$  from third-order structure functions  $D3(r)$ , extending the framework of Xie and Bühler

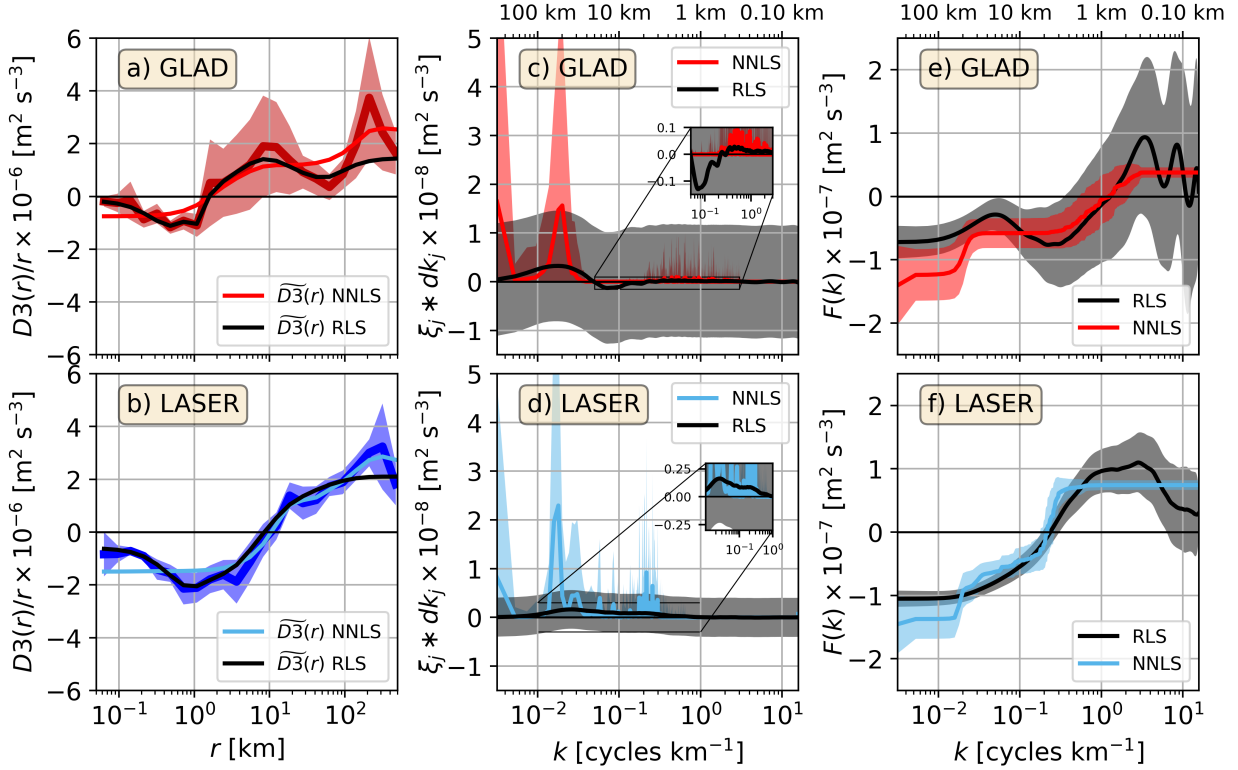


FIG. 11. (a)-(b) Normalized third-order structure function  $D3(r)/r$ , (c)-(d) KE injections rates  $\xi_j dk_j$  [ $\text{m}^2 \text{s}^{-3}$ ] and (e)-(f) KE transfers  $F(k)$  [ $\text{m}^2 \text{s}^{-3}$ ]. Dark red (a) and blue (b) solid lines show the structure function from GLAD (summer) and LASER (winter) datasets, respectively. Black solid line represents the variables estimated using RLS. Shaded areas in (a)-(b) are the prior uncertainties of  $D3(r)$ . Light red and blue solid lines show the NNLS-based results. Colored and gray-shaded areas are the NNLS-based bootstrapped standard error and the RLS posterior uncertainties, respectively. Positive and negative  $\xi_j$  in (c)-(d) indicate KE injection (divergence of KE transfer) and sink (convergence), respectively. Forward (downscale) and inverse (upscale) transfer are denoted by positive and negative  $F(k)$  in (e)-(f).  $k_j$  are linearly spaced with  $dk_j = 1/\max(r)$ . Small insets in (c) and (d) zoom in on the RLS-based injections.

(2019) and Balwada et al. (2022). The RLS method constrains the size of the fitted parameters by incorporating prior uncertainty and reduces overfitting, yielding physically realistic KE injection rates. In contrast, ordinary and non-negative least squares may produce unconstrained non-physical rates. Tests with a two-layer QG model that generates an eddy-rich mesoscale field show that RLS accurately captures the inverse energy transfer ( $F(k) < 0$ ) and the convergence of KE transfers

( $\xi_j < 0$ ) expected in QG turbulence (Figs. 6). In contrast, NNLS fails to detect convergences because it enforces only positive injection rates (Fig. 8).

Applied to the GLAD (summer) and LASER (winter) drifter datasets, both RLS and NNLS recover the expected bidirectional KE transfer, with  $F(k)$  transitioning from inverse to forward as  $k$  increases and the transition scale shifting seasonally from  $k \sim 1$  cycles  $\text{km}^{-1}$  in summer to  $k \sim 0.02$  cycles  $\text{km}^{-1}$  in winter (Fig. 11). However, only RLS identifies KE convergence ( $\xi_j < 0$ ) at intermediate scales ( $k \sim 0.07$  cycles  $\text{km}^{-1}$  in summer;  $k \sim 9 \times 10^{-3}$  cycles  $\text{km}^{-1}$  in winter), which enhances the inverse transfer and shifts the transition to forward transfer toward smaller scales. These convergences, undetected by NNLS, may arise from wind-driven damping (Renault et al. 2018), vertical KE transfer below the mixed layer, or conversion to potential energy, motivating future work combining this methodology with stratified turbulence diagnostics.

Adequately estimating the prior uncertainty in  $D3(r)$  is crucial for accurately estimating the KE transfer, as it has a significant impact on the posterior uncertainty in  $\xi_j$  and  $F(k)$ . An alternative approach for estimating prior uncertainties in  $D3(r)$  inherent in limited sampling settings is parametric bootstrapping, where the data are adjusted to a PDF such as a normal-inverse Gaussian distribution (DeMarco and Basu 2017; Barndorff-Nielsen et al. 2004) that best fits the data PDF (potentially using maximum likelihood estimation), and then bootstrapping is carried out using the adjusted data. This method has proved useful, yielding uncertainties in high-order structure functions with relatively less bias (DeMarco and Basu 2017). Additionally, the posterior uncertainty in  $\xi_j, \bar{\epsilon}$ , and  $F(k)$  could be improved by including a full error budget for the prior uncertainty in  $D3(r)$  accounting for sampling biases, instrument errors, and cross-correlations across observations (e.g., drifters; Spyrell et al. 2019).

This study demonstrates that the improved methodology, when combined with the  $D3(r)$  framework, can be applied to both gridded and sparse, ungridded datasets. In contrast, spectral and coarse-graining methods require gridded data to estimate velocity gradients (Srinivasan et al. 2023; Ajayi et al. 2021). Advective structure functions (Pearson et al. 2021) are particularly useful for estimating KE and enstrophy transfers in anisotropic flows, yet still require gridded data to calculate velocity gradients. Most ocean observations, such as drifters, shipboard acoustic Doppler current profiler transects, and autonomous platforms, provide ungridded velocity data, which can now be leveraged to quantify and analyze the KE transfer using the methodology presented here. A

deeper understanding of the KE transfer has the potential to refine existing ocean parameterizations and inspire new ones for global climate models.

*Data availability statement.* The code for the PyQG model is made available in <https://doi.org/10.5281/zenodo.6380711>, and documentation is available in <https://pyqg.readthedocs.io/en/latest/>. The GLAD and LASER experiment drifter data can be accessed in <https://data.gulfresearchinitiative.org/>. Python code for processing the GLAD and LASER drifter datasets, running the QG simulation, and estimating structure functions and spectral fluxes using regularized least-squares is available at [https://github.com/manuelogtzv/SF3\\_RLS](https://github.com/manuelogtzv/SF3_RLS). Arch 6.3.1 (Python library) used to estimate the moving-block bootstrapping (Shepard et al. 2024) is available in <https://arch.readthedocs.io/en/latest/index.html> and <https://zenodo.org/records/10981635>.

*Acknowledgments.* M. O. G. V., S. T. G., and M. M. have been supported by the NASA Surface Water and Ocean Topography Science Team (NASA 80NSSC20K1136, 80NSSC24K1657), the NASA Ocean Vector Winds Science Team (80NSSC19K0059, 80NSSC23K0979), and the NASA Ocean Surface Topography Science Team (80NSSC21K1822). D. B. acknowledges support from NSF grant OCE-2242110. B. C. acknowledges support from ONR grant N000142112726. M. M. acknowledges NASA grants 80GSFC20C0101 and NOAA grants NA23NOS4000334, NA20OAR4320278, and NA23OAR0110318. M. O. G. V. and D. B. acknowledge funding from NSF through the Learning the Earth with Artificial Intelligence and Physics (LEAP) Science and Technology Center (STC) (Award #2019625).

## APPENDIX A

### Equations for two-layer QG model

In this appendix, we provide details about the equations solved in the two-layer QG model (PyQG; Abernathey et al. 2022). The model uses QG potential vorticity in the upper  $q_1$  and lower  $q_2$  layers as prognostic variables:

$$q_m = \nabla^2 \Psi_m + (-1)^m F_m (\Psi_1 - \Psi_2), \quad m = 1, 2 \quad (\text{A1})$$

where  $\Psi_m$  is geostrophic streamfunction in layer  $m$  with thickness  $H_m$ ,  $F_1 = k_d^2 / (1 + \alpha)$ , and  $F_2 = \alpha F_1$ , where

$$k_d^2 = \frac{f_o^2}{g'} \frac{H_1 + H_2}{H_1 H_2} \quad (\text{A2})$$

is the baroclinic Rossby deformation wavenumber,  $\alpha = H_1 / H_2$  is the layer thickness ratio,  $f_o$  is the local Coriolis frequency, and  $g'$  is reduced gravity.  $\Psi_m$  is diagnosed from  $q_m$  by integrating the Laplacian using periodic boundary conditions. The horizontal velocity components are calculated using the  $\Psi_m$ :

$$u_m = -\partial_y \Psi_m, \quad v_m = \partial_x \Psi_m. \quad (\text{A3})$$

The model solves the evolution of the QG potential vorticity field in spectral space  $\Psi_m = \sum \widehat{\Psi}_m e^{i(k_x \cdot x + k_y \cdot y)}$ :

$$\partial_t \widehat{q}_m = -\widehat{J}(\Psi_m, q_m) - i k_x \beta \widehat{\Psi}_m - i k_x U_m \widehat{\Psi}_m + \delta_{m,2} r_{ek} k^2 \widehat{\Psi}_2 + \widehat{\text{SSD}}, \quad (\text{A4})$$

where  $U_m$  is the background flow,  $\partial_t$  is the Eulerian time derivative, and  $J(\Psi_m, q_m) = \partial_x \Psi_m \partial_y q_m - \partial_y \Psi_m \partial_x q_m$  is the Jacobian in physical space. The change in the Coriolis frequency with latitude  $y$  is defined as  $f_o + \beta y$  with a slope  $\beta$ .  $\delta_{m,2}$  is the Kronecker delta function, and  $r_{ek}$  is the bottom drag coefficient applied only to the second layer to dissipate large-scale energy. The small-scale dissipation, SSD, absorbs enstrophy that cascades toward small scales and is set as an exponential filter:

$$E_f(k^*) = \begin{cases} 1 & k^* < k_c \\ e^{-23.6(k^* - k_c)^4}, & k^* \geq k_c \end{cases}, \quad (\text{A5})$$

where  $k^* = \sqrt{(k_x \Delta x)^2 + (k_y \Delta y)^2}$  is the non-dimensional wavenumber,  $\Delta x = \Delta y = 3.9$  km are the spatial grid spacing, and  $k_c = 0.65\pi$  is the non-dimensional cut-off wavenumber. The filter reduces aliasing errors and provides stable simulations with necessary numerical dissipation (Ross et al. 2023), and attenuates the highest third of wavenumbers of all terms in the right side of (A4). More details about the model's solution are found in Abernathey et al. (2022).

## APPENDIX B

### Second-order structure function and degrees of freedom

Here we show the second-order structure function  $D2(r)$  and the degrees of freedom estimated from the QG model  $u, v$  outputs, and the drifter data. We follow Balwada et al. (2022) and employ  $D2(r)$  to estimate the degrees of freedom  $N(r)$  as

$$T_{scale}(r) = r / \sqrt{D2(r)}, \quad (B1)$$

$$N(r) = T_{tot} / T_{scale}(r), \quad (B2)$$

where  $T_{tot}$  is the duration of the model's time series used for the analysis (5 years) and 90 and 60 days for the summer GLAD and wintertime LASER drifter data sets, respectively.

### QG model

We transform  $E(k)$  (blue solid, Fig. 3a) to second-order structure function  $D2(r)$  via (4) and compare it to  $D2(r)$  calculated directly from the model's velocity output (Fig. B1a). The theoretical  $D2$  (blue solid) lies on top of the estimated  $D2$  (black solid) and within the spatially-averaged estimates  $\overline{\delta u^2}(r, t)$  (red solid) (Fig. B1a) following a  $r^2$  power law for  $r \leq 20$  km. The theoretical and estimated  $D2(r)$  show a shallower  $r$  relationship for  $30 \text{ km} < r < 70 \text{ km}$ . We used  $D2(r)$  to estimate  $T_{scale}(r)$  with (B1) and  $N(r)$  via (B2); the latter is employed to estimate the uncertainty in  $D3(r)$ . As expected, larger flows decorrelate more slowly than small-scale flows (black solid); consequently,  $N(r)$  decreases with  $r$  (red solid) (Fig. B1b).

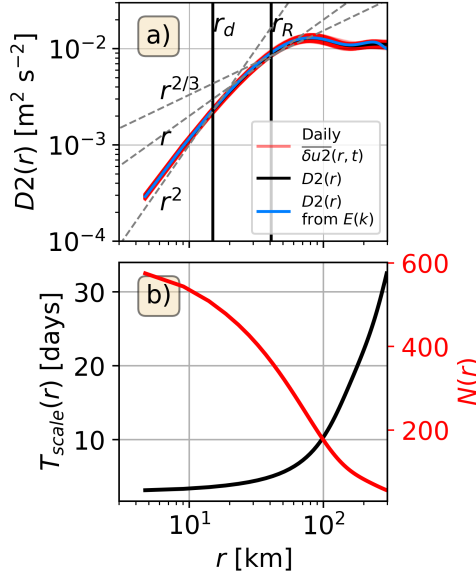


FIG. B1. (a) Second-order structure function  $D2(r)$  [ $\text{m}^2 \text{s}^{-2}$ ]. Red solid lines represent daily estimates  $\overline{\delta u^2}(r, t)$ . Black and blue solid lines are the five-year mean  $D2(r)$  and the structure function estimated from  $E(k)$ , respectively. Power laws are shown in dashed gray lines. Vertical solid lines show the model's  $r_d$  and Rhine's scale  $r_R = 1/k_d$ . (b) Decorrelation time scale  $T_{scale}(r)$  [days] (black line; left y-axis) and degrees of freedom  $N(r)$  (red line; right y-axis) estimated using (B1) and (B2), respectively and setting  $T_{tot} = 5$  years.

### Drifter data

Following Balwada et al. (2022), we estimated  $D2(r)$  by replacing the ensemble averaging of  $\delta u^2(\mathbf{s}, \mathbf{r}, t)$  by averaging all samples per  $r$  bin. Submesoscales with scales  $r < 10$  km are more energetic during the winter (blue solid) than in summer (red solid), whereas mesoscales ( $r > 10$  km) are more energetic during the summer than winter (Fig. B2a). The energizing of submesoscales in winter is likely driven by energetic submesoscale mixed layer instabilities that convert potential energy stored in the winter deep mixed layer to KE at the scales of the mixed layer deformation radius (Callies et al. 2015; Balwada et al. 2022). As in the model,  $T_{scale}(r)$  estimated using (B1) increases linearly with  $r$  in log-log space (red and blue solid, Fig. B2b). At submesoscales, summertime  $T_{scale}$  (red solid) exhibits slightly shorter  $T_{scale}(r)$  than wintertime (blue solid).  $N(r)$  decreases with  $r$  with summertime (red dotted) having slightly more  $N(r)$  than in winter (blue dotted) (except for  $10^{-1} \text{ km} < r < 10^1 \text{ km}$ ) as the summertime experiment's duration is larger than that in winter (Fig. B2b).

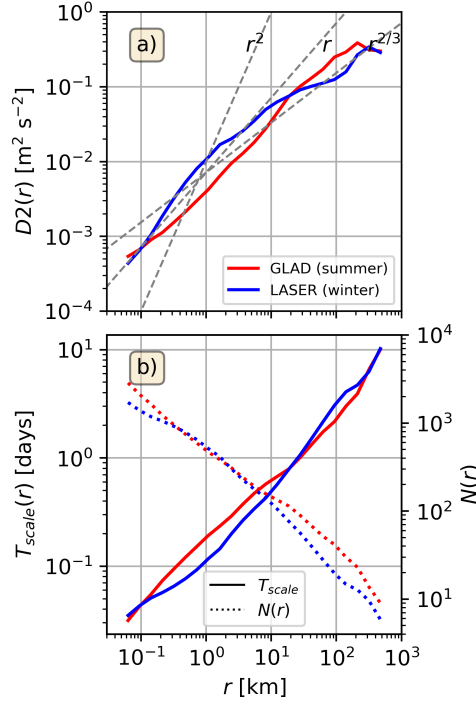


FIG. B2. (a) Second-order structure function  $D2(r)$  [ $\text{m}^2 \text{s}^{-2}$ ] for the GLAD (red solid line) and LASER (blue solid line) experiments. Power laws are shown in dashed gray. (b) Decorrelation time scale  $T_{scale}(r)$  [days] (solid lines) and degrees of freedom  $N(r)$  (dotted lines) estimated by setting  $T_{tot} = 90$  days and 60 days for the GLAD and LASER experiments, respectively.

## APPENDIX C

### First-order structure function

An important requirement for the structure-function theory is that the flow must be homogeneous, i.e.,  $D1(r) = 0$  for any length scale  $r$  (Frisch 1995). The mean current can determine the sign and magnitude of the  $D3(r)$ , limiting the application of the  $D3(r)$  framework. In this appendix, we calculated  $D1(r)$  from the velocity fields in the model and drifter data using (3) to analyze whether the homogeneity condition is fulfilled.

#### Two-layer QG model

Daily  $\overline{\delta u1}(r, t)$  is shown in Fig. C1a along with the five-year ensemble averaged  $D1(r)$ . The daily snapshots (orange solid) variability increases with separation  $r$ . The mean  $D1(r)$  (black

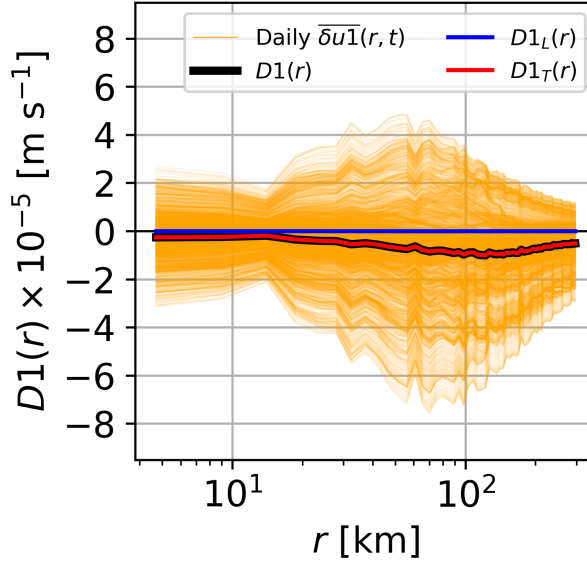


FIG. C1. Upper-layer five-year first-order structure function  $D1(r)$  [ $\text{m s}^{-1}$ ]. Orange lines are daily  $\overline{\delta u1}(r, t)$ . Black, blue, and red solid lines are the five-year ensemble-averaged  $D1$ , longitudinal  $D1_L(r)$ , and transverse  $D1_T(r)$  structure functions.

solid) is almost zero for  $r < 20$  km but becomes statistically different from zero at the larger scales. Since the longitudinal component is linked to divergent flows (Pearson et al. 2020), the five-year mean longitudinal structure function  $D1_L(r)$  (blue solid) vanishes because the model flow field is purely rotational, as expected in QG flows. Consequently, only the transverse component  $D1_T(r)$  (red solid) contributes to the total structure function  $D1(r)$ .

### Drifter data

First-order structure function  $D1(r)$  (Fig. C2) for the GLAD (summer; red solid) and LASER (winter; blue solid) datasets show that the background flow has a large contribution across different flow scales, with a larger contribution at the mesoscales ( $r \sim \mathcal{O}(10^2)$  km) and during wintertime. Surface drifters converging into individual flow features such as mesoscale eddies and large-scale currents (Fig. 1) could result in highly heterogeneous sampling (Pearson et al. 2020).

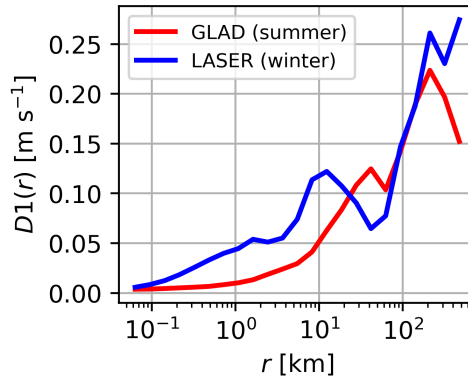


FIG. C2. First-order structure function  $D1(r)$  [m s<sup>-1</sup>] for the GLAD (summer; red solid line) and LASER (winter; blue solid line) experiments.

## References

- Abernathy, R., and Coauthors, 2022: PyQG. Zenodo, doi:<https://doi.org/10.5281/zenodo.6563667>.
- Ajayi, A., J. Le Sommer, E. P. Chassignet, J.-M. Molines, X. Xu, A. Albert, and W. Dewar, 2021: Diagnosing Cross-Scale Kinetic Energy Exchanges From Two Submesoscale Permitting Ocean Models. *Journal of Advances in Modeling Earth Systems*, **13** (6), e2019MS001923, doi:<https://doi.org/10.1029/2019MS001923>.
- Aluie, H., M. Hecht, and G. K. Vallis, 2018: Mapping the energy cascade in the North Atlantic Ocean: The coarse-graining approach. *Journal of Physical Oceanography*, **48** (2), 225 – 244, doi:10.1175/JPO-D-17-0100.1.
- Balwada, D., J. H. LaCasce, and K. G. Speer, 2016: Scale-dependent distribution of kinetic energy from surface drifters in the gulf of mexico. *Geophysical Research Letters*, **43** (20), 10–856.
- Balwada, D., Q. Xiao, S. Smith, R. Abernathy, and A. R. Gray, 2021: Vertical fluxes conditioned on vorticity and strain reveal submesoscale ventilation. *Journal of Physical Oceanography*, **51** (9), 2883–2901.
- Balwada, D., J.-H. Xie, R. Marino, and F. Feraco, 2022: Direct observational evidence of an oceanic dual kinetic energy cascade and its seasonality. *Science Advances*, **8** (41), eabq2566, doi:10.1126/sciadv.abq2566.

- Barndorff-Nielsen, O. E., P. Blæsild, and J. Schmiegel, 2004: A parsimonious and universal description of turbulent velocity increments. *The European Physical Journal B-Condensed Matter and Complex Systems*, **41** (3), 345–363, doi:<https://doi.org/10.1140/epjb/e2004-00328-1>.
- Bennett, A. F., 1984: Relative dispersion: Local and nonlocal dynamics. *Journal of Atmospheric Sciences*, **41** (11), 1881 – 1886, doi:10.1175/1520-0469(1984)041<1881:RDLAND>2.0.CO;2.
- Callies, J., R. Ferrari, J. M. Klymak, and J. Gula, 2015: Seasonality in submesoscale turbulence. *Nature communications*, **6** (1), 6862, doi:<https://doi.org/10.1038/ncomms7862>.
- Capet, X., J. C. McWilliams, M. J. Molemaker, and A. F. Shchepetkin, 2008: Mesoscale to Submesoscale Transition in the California Current System. Part III: Energy Balance and Flux. *Journal of Physical Oceanography*, **38** (10), 2256 – 2269, doi:10.1175/2008JPO3810.1, URL <https://journals.ametsoc.org/view/journals/phoc/38/10/2008jpo3810.1.xml>.
- Cho, J. Y. N., and E. Lindborg, 2001: Horizontal velocity structure functions in the upper troposphere and lower stratosphere: 1. Observations. *Journal of Geophysical Research: Atmospheres*, **106** (D10), 10 223–10 232, doi:10.1029/2000JD900814.
- DeMarco, A. W., and S. Basu, 2017: Estimating higher-order structure functions from geophysical turbulence time series: Confronting the curse of the limited sample size. *Physical Review E*, **95** (5), 052 114, doi:<https://doi.org/10.1103/PhysRevE.95.052114>.
- Dong, J., B. Fox-Kemper, H. Zhang, and C. Dong, 2020: The seasonality of submesoscale energy production, content, and cascade. *Geophysical Research Letters*, **47** (6), e2020GL087 388, doi: <https://doi.org/10.1029/2020GL087388>.
- Ferrari, R., and C. Wunsch, 2009: Ocean circulation kinetic energy: Reservoirs, sources, and sinks. *Annual Review of Fluid Mechanics*, **41** (1), 253–282.
- Freilich, M., L. Lenain, and S. T. Gille, 2023: Characterizing the role of non-linear interactions in the transition to submesoscale dynamics at a dense filament. *Geophysical Research Letters*, **50** (15), e2023GL103 745, doi:<https://doi.org/10.1029/2023GL103745>.
- Frisch, U., 1995: *Turbulence: the legacy of AN Kolmogorov*. Cambridge university press.
- Hansen, P. C., 1999: The L-curve and its use in the numerical treatment of inverse problems.

- 781 Kachelein, L., B. D. Cornuelle, S. T. Gille, and M. R. Mazloff, 2022: Harmonic analysis of  
782 non-phase-locked tides with red noise using the red tide package. *Journal of Atmospheric and*  
783 *Oceanic Technology*, **39** (7), 1031 – 1051, doi:<https://doi.org/10.1175/JTECH-D-21-0034.1>.
- 784 Kolmogorov, A. N., 1991: The local structure of turbulence in incompressible viscous fluid for very  
785 large Reynolds numbers. *Proceedings of the Royal Society of London. Series A: Mathematical*  
786 *and Physical Sciences*, **434** (1890), 9–13.
- 787 Kunsch, H. R., 1989: The Jackknife and the Bootstrap for General Stationary Observations. *The*  
788 *Annals of Statistics*, **17** (3), 1217 – 1241, doi:[10.1214/aos/1176347265](https://doi.org/10.1214/aos/1176347265), URL [https://doi.org/10.](https://doi.org/10.1214/aos/1176347265)  
789 [1214/aos/1176347265](https://doi.org/10.1214/aos/1176347265).
- 790 Lindborg, E., 1999: Can the atmospheric kinetic energy spectrum be explained by two-dimensional  
791 turbulence? *Journal of Fluid Mechanics*, **388**, 259–288, doi:[10.1017/S0022112099004851](https://doi.org/10.1017/S0022112099004851).
- 792 Lindborg, E., and J. Y. N. Cho, 2001: Horizontal velocity structure functions in the upper tropo-  
793 sphere and lower stratosphere: 2. Theoretical considerations. *Journal of Geophysical Research:*  
794 *Atmospheres*, **106** (D10), 10 233–10 241, doi:<https://doi.org/10.1029/2000JD900815>.
- 795 Naveira Garabato, A. C., X. Yu, J. Callies, R. Barkan, K. L. Polzin, E. E. Frajka-Williams,  
796 C. E. Buckingham, and S. M. Griffies, 2022: Kinetic energy transfers between mesoscale and  
797 submesoscale motions in the open ocean’s upper layers. *Journal of Physical Oceanography*,  
798 **52** (1), 75–97, doi:[10.1175/JPO-D-21-0099.1](https://doi.org/10.1175/JPO-D-21-0099.1).
- 799 Pearson, B. C., J. L. Pearson, and B. Fox-Kemper, 2021: Advective structure functions  
800 in anisotropic two-dimensional turbulence. *Journal of Fluid Mechanics*, **916**, A49, doi:  
801 [10.1017/jfm.2021.247](https://doi.org/10.1017/jfm.2021.247).
- 802 Pearson, J., B. Fox-Kemper, R. Barkan, J. Choi, A. Bracco, and J. C. McWilliams, 2019: Impacts  
803 of convergence on structure functions from surface drifters in the Gulf of Mexico. *Journal of*  
804 *Physical Oceanography*, **49** (3), 675–690, doi:<https://doi.org/10.1175/JPO-D-18-0029.1>.
- 805 Pearson, J., and Coauthors, 2020: Biases in structure functions from observations of submesoscale  
806 flows. *Journal of Geophysical Research: Oceans*, **125** (6), e2019JC015 769, doi:[https://doi.org/](https://doi.org/10.1029/2019JC015769)  
807 [10.1029/2019JC015769](https://doi.org/10.1029/2019JC015769).

- Poje, A. C., T. M. Özgökmen, D. J. Bogucki, and A. Kirwan, 2017: Evidence of a forward energy cascade and kolmogorov self-similarity in submesoscale ocean surface drifter observations. *Physics of Fluids*, **29** (2).
- Qiu, B., T. Nakano, S. Chen, and P. Klein, 2022: Bi-directional energy cascades in the Pacific Ocean from equator to Subarctic Gyre. *Geophysical Research Letters*, **49** (8), e2022GL097713, doi:10.1029/2022GL097713.
- Renault, L., J. C. McWilliams, and J. Gula, 2018: Dampening of submesoscale currents by air-sea stress coupling in the californian upwelling system. *Scientific reports*, **8** (1), 13388, doi:https://doi.org/10.1038/s41598-018-31602-3.
- Ross, A., Z. Li, P. Perezhogin, C. Fernandez-Granda, and L. Zanna, 2023: Benchmarking of Machine Learning Ocean Subgrid Parameterizations in an Idealized Model. *Journal of Advances in Modeling Earth Systems*, **15** (1), e2022MS003258, doi:https://doi.org/10.1029/2022MS003258.
- Sasaki, H., P. Klein, Y. Sasai, and B. Qiu, 2017: Regionality and seasonality of submesoscale and mesoscale turbulence in the north pacific ocean. *Ocean Dynamics*, **67**, 1195–1216.
- Schubert, R., J. Gula, R. J. Greatbatch, B. Baschek, and A. Biastoch, 2020: The Submesoscale Kinetic Energy Cascade: Mesoscale Absorption of Submesoscale Mixed Layer Eddies and Frontal Downscale Fluxes. *Journal of Physical Oceanography*, **50** (9), 2573 – 2589, doi:https://doi.org/10.1175/JPO-D-19-0311.1.
- Schubert, R., O. Vergara, and J. Gula, 2023: The open ocean kinetic energy cascade is strongest in late winter and spring. *Communications Earth & Environment*, **4** (1), 450, doi:https://doi.org/10.1038/s43247-023-01111-x.
- Scott, R. B., and F. Wang, 2005: Direct evidence of an oceanic inverse kinetic energy cascade from satellite altimetry. *Journal of Physical Oceanography*, **35** (9), 1650–1666.
- Sheppard, K., and Coauthors, 2024: bashtage/arch: Release 7.0.0. Zenodo, URL https://doi.org/10.5281/zenodo.10981635, doi:10.5281/zenodo.10981635.
- Spydell, M. S., F. Feddersen, and J. Macmahan, 2019: The effect of drifter gps errors on estimates of submesoscale vorticity. *Journal of Atmospheric and Oceanic Technology*, **36** (11), 2101–2119, doi:10.1175/JTECH-D-19-0108.1.

- 836 Srinivasan, K., R. Barkan, and J. C. McWilliams, 2023: A forward energy flux at submesoscales  
 837 driven by frontogenesis. *Journal of Physical Oceanography*, **53** (1), 87 – 305, doi:[https://doi.](https://doi.org/10.1175/JPO-D-22-0001.1)  
 838 [org/10.1175/JPO-D-22-0001.1](https://doi.org/10.1175/JPO-D-22-0001.1).
- 839 Steinberg, J. M., S. T. Cole, K. Drushka, and R. P. Abernathey, 2022: Seasonality of the mesoscale  
 840 inverse cascade as inferred from global scale-dependent eddy energy observations. *Journal of*  
 841 *Physical Oceanography*, **52** (8), 1677–1691.
- 842 Storer, B. A., M. Buzzicotti, H. Khatri, S. M. Griffies, and H. Aluie, 2023: Global cascade of  
 843 kinetic energy in the ocean and the atmospheric imprint. *Science Advances*, **9** (51), eadi7420.
- 844 Stroock, D. W., 2010: *Probability theory: an analytic view*. Cambridge university press.
- 845 Tedesco, P. F., L. E. Baker, A. C. N. Garabato, M. R. Mazloff, S. T. Gille, C. P. Caulfield, and  
 846 A. Mashayek, 2024: Spatiotemporal Characteristics of the Near-Surface Turbulent Cascade  
 847 at the Submesoscale in the Drake Passage. *Journal of Physical Oceanography*, **54** (1), 187 –  
 848 215, doi:10.1175/JPO-D-23-0108.1, URL [https://journals.ametsoc.org/view/journals/phoc/54/](https://journals.ametsoc.org/view/journals/phoc/54/1/JPO-D-23-0108.1.xml)  
 849 [1/JPO-D-23-0108.1.xml](https://journals.ametsoc.org/view/journals/phoc/54/1/JPO-D-23-0108.1.xml).
- 850 Uchida, T., Q. Jamet, A. C. Poje, N. Wienders, W. K. Dewar, and B. Deremble, 2023: Wavelet-  
 851 based wavenumber spectral estimate of eddy kinetic energy: Idealized quasi-geostrophic flow.  
 852 *Journal of Advances in Modeling Earth Systems*, **15** (3), e2022MS003 399.
- 853 Vallis, G. K., 2017: *Atmospheric and oceanic fluid dynamics*. Cambridge University Press.
- 854 Wunsch, C., 1996: *The Ocean Circulation Inverse Problem*. Cambridge University Press, Cam-  
 855 bridge, 437 pp.
- 856 Xie, J.-H., and O. Bühler, 2019: Third-order structure functions for isotropic turbulence with  
 857 bidirectional energy transfer. *Journal of Fluid Mechanics*, **877**, R3, doi:10.1017/jfm.2019.651.
- 858 Yu, X., R. Barkan, and A. C. Naveira Garabato, 2024: Intensification of submesoscale frontogenesis  
 859 and forward energy cascade driven by upper-ocean convergent flows. *Nature Communications*,  
 860 **15** (1), 9214, doi:<https://doi.org/10.1038/s41467-024-53551-4>.
- 861 Zhang, Z., and Coauthors, 2023: Submesoscale inverse energy cascade enhances southern ocean  
 862 eddy heat transport. *nature communications*, **14** (1), 1335.